Targeted and activatable nanosystem for fluorescent and optoacoustic imaging of immune-mediated inflammatory diseases and therapy via inhibiting NF-κB/NLRP3 pathways

Lihe Sun [1], Juan Ouyang [1], Zhuo Zeng, Cheng Zeng, Yunqing Ma, Fang Zeng [**], Shuizhu Wu [*]

Biomedical Division, State Key Laboratory of Luminescent Materials and Devices, Guangdong Provincial Key Laboratory of Luminescence from Molecular Aggregates, College of Materials Science and Engineering, South China University of Technology, Guangzhou, 510640, China

ARTICLE INFO

ABSTRACT

Immune-mediated inflammatory diseases (IMIDs) represent a diverse group of diseases and challenges remain for the current medications. Herein, we present an activatable and targeted nanosystem for detecting and imaging IMIDs foci and treating them through blocking NF-κB/NLRP3 pathways. A ROS-activatable prodrug BH-EGCG is synthesized by coupling a near-infrared chromophore with the NF-κB/NLRP3 inhibitor epigallocatechin-3-gallate (EGCG) through boronate bond which serves as both the fluorescence quencher and ROS-responsive moiety. BH-EGCG molecules readily form stable nanoparticles in aqueous medium, which are then coated with macrophage membrane to ensure the actively-targeting capability toward inflammation sites. Additionally, an antioxidant precursor N-acetylcysteine is co-encapsulated into the coated nanoparticles to afford the nanosystem BH-EGCG&NAC@MM to further improve the anti-inflammatory efficacy. Benefiting from the inflammation-homing effect of the macrophage membrane, the nanosystem delivers payloads (diagnostic probe and therapeutic drugs) to inflammatory lesions more efficiently and releases a chromophore and two drugs upon being triggered by the overexpressed in-situ ROS, thus exhibiting better theranostic performance in the autoimmune hepatitis and hind paw edema mouse models, including more salient imaging signals and better therapeutic efficacy via inhibiting NF-κB pathway and suppressing NLRP3 inflammasome activation. This work may provide perceptions for designing other actively-targeting theranostic nanosystems for various inflammatory diseases.

1. Introduction

Immune-mediated inflammatory diseases (IMIDs) represent a diverse group of chronic inflammatory and autoimmune disorders that share common inflammatory pathways [1–3]. The etiology of these complex diseases is multifactorial, including environmental, microbial, immune and genetic factors, resulting in immune dysregulation and excessive inflammation in the affected organs. IMIDs affect around 3%–7% of the population [4], and accumulating data have shown that a patient with IMID has an increased risk of developing another IMID [5, 6].

The immune dysregulation results in self-perpetuating of inflammation and leads to a variety of inflammatory diseases such as immune-mediated hepatitis, rheumatoid arthritis (RA), Crohn's disease (CD), asthma, ulcerative colitis (UC) and others [7–14]. For example, autoimmune hepatitis is a liver inflammation in which the immune system attacks liver cells and induces the hepatitis. If not treated, this disease can become quite serious and get worse over time, and eventually lead to hepatic cirrhosis and/or liver failure. When diagnosed and treated early, however, autoimmune hepatitis often can be controlled with drugs that suppress the immune system. Therefore, early detection, prevention and treatment of excessive inflammation or severe chronic inflammation are of great importance in reducing the risks of chronic inflammatory diseases and promoting the healing process.

The therapeutic options for patients with immune-mediated inflammatory diseases have improved over the past two decades through
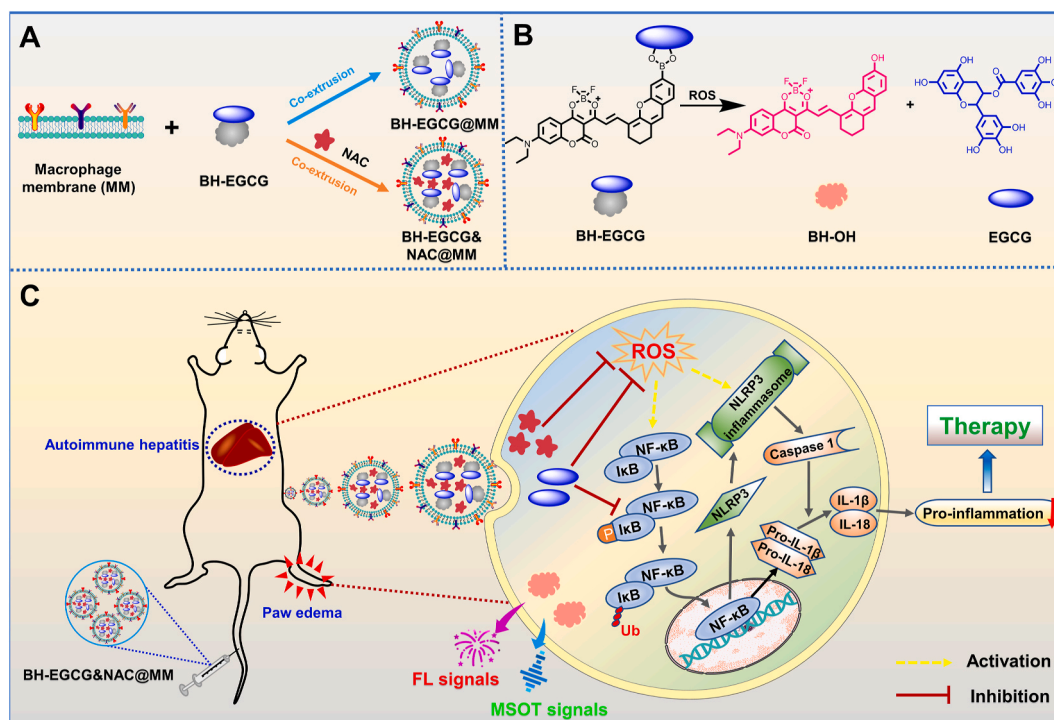

Fig. 1. Schematic representations of BH-EGCG&NAC@MM nanosystem for inflammatory diseases' theranostics. (A) Scheme displaying the preparation of BH-EGCG@MM and BH-EGCG&NAC@MM using extrusion method. (B) The response mechanism of BH-EGCG toward ROS. (C) Scheme showing multiple actions of BH-EGCG&NAC@MM, including diagnosis of ConA-induced autoimmune hepatitis and CAR-induced hind paw edema via NIR fluorescent imaging and optoacoustic imaging, and efficient therapy of ConA-induced acute autoimmune hepatitis and CAR-induced hind paw edema via inhibiting NF-κB pathway and suppressing NLRP3 inflammasome formation.

introduction of several novel medications, in particular biological disease-modifying antirheumatic drugs (DMARDs) [15,16], drugs targeting cytokines (e.g. tumor necrosis factor and interferons) [7,17,18], and Janus kinase (JAK)-inhibitors [19,20], as well as drugs targeting immune cells [21]. However, some immune-mediated inflammatory diseases are notoriously difficult to treat, and challenges remain for the current medications, such as low selectivity and efficacy, toxicity and off-target [7], hence there is still room for improvement in IMID treatment.

Recently, inflammasomes, the cytoplasmic multi-protein complexes, have been identified as the critical component of innate immune system which assemble in response to danger signals (including bacteria, virus as well as infection-unrelated signals such as ROS) and initiate some pro-inflammatory cytokines' release (such as IL-1β and IL-18) for inflammatory responses' activation [22–24]. Inflammasome activation has been investigated in a number of immunity-related diseases, and aberrant activation of inflammasome has been identified as a main contributor to a variety of inflammatory diseases, autoimmune diseases and central nervous system disorders [23–25]. The NLRP3 inflammasome is a relatively well-studied inflammasome and has been identified as a potential mediator of a wide range of immune-related diseases, and application of potent inhibitor for NLPR3 activation signifies a rational curative strategy to cure these diseases or disorders [25–28]. More importantly, NLRP3 inflammasome can be activated by many and diverse stimuli, thus making NLRP3 the most versatile and also the most clinically implicated inflammasome as a regulatory node of oxidative stress and inflammatory diseases [28]. To date, a lot of NLRP3 inhibitors have been identified or developed for immune disease treatment [29]. Epigallocatechin-3-gallate (EGCG) is a natural polyphenolic compound (antioxidant) in green tea and has been identified as a specific inhibitor which blocks the activation of nuclear factor-κB (NF-κB) [30,31]. NF-κB is a transcription factor and key regulator of genes coding for inflammatory mediators, it plays a crucial role in the expression of NLRP3

protein and some inflammatory cytokine precursors (e.g. pro-IL-1β and pro-IL-18) in priming step of NLRP3 inflammasome formation [32]. Accordingly, EGCG has been identified and employed as an inhibitor for NLRP3 inflammasome [33–35].

Effective delivery and subsequent on-demand release of inhibitor of NLRP3 inflammasome at the disease site would be conducive to precision therapy of IMID. There have been a number of targeting strategies to deliver or guide the therapeutic drugs to inflammatory sites [36–38], and cell-membrane coating has recently emerged as a potential way for drug delivery [39–42]. Macrophages are a type of white blood cells in the immune system and represent the major cellular effector in inflammation, and they have innate ability of being recruited to the site of inflammatory disease, and they can target the inflammatory site because of their inflammation-chemotactic and homing property. Hence, the macrophage-membrane-coated nanodrugs can actively target the inflammatory sites, while immune detection of them can be averted with sustained circulation. This strategy therefore displays great potential for targeting and treating inflammation-related diseases.

Oxidative stress (upregulation of reactive oxygen species (ROS)) is known to be involved in and promotes the pathogenesis and development of inflammatory diseases [43–45]. At the site of inflammation there is an enhanced level of ROS generation, which leads to DNA damages in endothelial dysfunction and tissue injuries. Excessive and uncontrolled inflammation is deleterious and results in a variety of inflammatory diseases. The overexpressed ROS can not only serve as the biomarker for inflammatory diseases, but also the driving force for activating a prodrug for treating various inflammatory diseases, including allergies, autoimmune diseases and metabolic disorders [46–50].

Moreover, targeted nanodrugs which can give out indicative signals upon activation by ROS would be an ideal theranostic system for in-situ detection of inflammation-related diseases in a non-invasive manner and for on-demand drug release in the disease site, thereby offering

accurate diagnosis and precision treatment. Near infrared (NIR) fluorescence imaging technology has been established as a powerful tool for providing a high degree of sensitivity in biomedical applications due to its attractive properties such as high contrast and sensitivity, low cost, absence of ionizing radiation, ease of use, and high specificity [50–56]. Recently, to further improve the performance of the optical imaging, such as the elevation of penetration depth and reduction of tissue scattering, the optoacoustic imaging has emerged as a robust and promising modality for live animal imaging [57–63]. In particular, multispectral optoacoustic tomography (MSOT), which functions by illuminating a sample with NIR laser pulses of multiple wavelengths and collecting the ultrasound signals emitted by various photoabsorbers in the sample, can acquire wavelength-specific optoacoustic spectrum for a particular absorber and achieve both tomographic and three-dimensional images, which ensures accurate pinpointing of disease site in a spatiotemporal and non-invasive manner [57–63].

Taken together, we aim to develop a ROS-activatable and targeted nanosystem for detecting and imaging inflammatory disease foci and treating immune-mediated inflammatory diseases through blocking NF-κB/NLRP3 pathways (Fig. 1). A boric acid-containing NIR chromophore was designed and synthesized, and then coupled with a NF-κB/NLRP3 inhibitor epigallocatechin-3-gallate (EGCG), forming a theranostic prodrug (BH-EGCG). The pathological levels of ROS in the inflammatory disease site could cleave the boronate ester bond between the chromophore and EGCG, thereby releasing the active drug for therapy and the chromophore for NIR fluorescence and MSOT imaging. The BH-EGCG molecules formed stable nanoparticles in aqueous medium, and were then coated with macrophage cell membrane, during which an antioxidant precursor and ROS scavenger N-acetylcysteine (NAC) was also loaded into the nanosystem to further enhance the therapeutic efficacy. The multi-functionality of the nanosytem were evaluated on two NF-κB-associated IMID mouse models (concanavalin A (ConA)-induced autoimmune hepatitis model and the carrageenan (CAR)-induced hind paw edema model); and the relevant results manifest the nanosystem's targetability to disease foci, dual-mode (fluorescence and optoacoustic) imaging capability, on-site drug release of active drugs, as well as high therapeutic efficacy against the two IMIDs via inhibiting NF-κB/NLRP3 pathways. To the best of our knowledge, this is the first study on the macrophage membrane-coated theranostic nanosystem's applications in IMIDs mouse models.

2. Materials and methods

2.1. Preparation and characterization of BH-EGCG, BH-EGCG@MM and BH EGCG&NAC@MM nanoparticles

The molecular prodrug BH-EGCG (a chromophore-EGCG dyad) was synthesized according to a procedure outlined in Scheme S1 in Supporting Information, and the detailed synthesis processes are presented in the Supporting Information.

To prepare nanoparticles, the stock solution of BH-EGCG in DMSO at a concentration of 1 mM was added dropwise into 10 mL triple-distilled water and sonicated at 4 °C for 10 min. As BH-EGCG is amphiphilic, BH-EGCG molecules readily form nanoparticles in aqueous media. Afterwards, the solution is dialyzed against distilled water to remove the unself-assembled molecules and DMSO with a dialysis bag (cut-off molecular weight: 500 Da). The obtained BH-EGCG nanoparticles were immediately used for subsequent experiments.

To obtain macrophage membrane, RAW 264.7 cells were harvested with EDTA PBS solution (2 mM) and resuspended in pre-cool Tris-magnesium buffer (TM buffer, pH 7.4, 0.01 M Tris and 0.001 M MgCl) at a cell density of 2.5×10^7 cells mL^{-1}. Afterwards, cells were extruded through a mini-extruder (Avestin, LF-1, Canada) for 20 times without a polycarbonate membrane to disrupt the cells. The cell homogenate was mixed with 1 M sucrose at a final concentration of 0.25 M sucrose, and then centrifuged at 2000 g and 4 °C for 10 min. The collected

supernatant was further centrifuged at 20000 g and 4 °C for 30 min. Then, the pellet was discarded and the supernatant was centrifuged at 25000 g and 4 °C for another 2 h with the aid of ultra-speed centrifuge (LE-80K, Beckman Coulter). Finally, the pellet was collected and freeze-dried as purified macrophage membrane, and stored at −80 °C for subsequent use.

BH-EGCG@MM nanoparticles were prepared by coating the prepared BH-EGCG nanoparticles with macrophage membrane. Briefly, the purified macrophage membrane from 1×10^8 cells was mixed with the prepared BH-EGCG nanoparticles solution (1 mL), and the mixture was repeatedly extruded for 11 times through a polycarbonate membrane (pore size: 400 nm) on the mini-extruder. The excess cell membrane was removed by centrifugation at 2000g and 4 °C for 10 min. Finally, the newly macrophage membrane-coated nanoparticles (BH-EGCG@MM nanoparticles) were freeze-dried and stored at −20 °C for further use.

For the preparation of BH-EGCG&NAC@MM nanoparticles, NAC (1 mg) was added into the mixture of BH-EGCG nanoparticles (2 mg) with purified cell membrane (from 1×10^8 cells), and the mixture was repeatedly extruded for 11 times through a polycarbonate membrane (pore size: 400 nm) on the mini-extruder. The excess cell membrane was removed by centrifugation at 2000g and 4 °C for 10 min. Finally, the newly macrophage membrane-coated nanoparticles (BH-EGCG&NAC@MM nanoparticles) were freeze-dried and stored at −20 °C for further use.

2.2. Characterization of the nanoparticles

In order to confirm the successful coating of the macrophage membrane, transmission electron microscopy (TEM) observation and dynamic light scattering (DLS) measurement were conducted to characterize the morphology and measure the particle size distribution of the nanoparticles, respectively.

The sodium dodecyl sulfate-polyacrylamide gel electrophoresis (SDS-PAGE) experiment was conducted to analyze the protein profiles in the macrophage membrane and the nanoparticles. The proteins in macrophage membrane and the nanoparticles, including BH-EGCG, BH-EGCG@MM and BH-EGCG&NAC@MM, were extracted out with RIPA lysis buffer supplemented with protease inhibitor and quantified by a BCA assay. The protein samples were then mixed with 5X loading buffer before heating at 100 °C for 5 min. Each well in the 4%–20% SurePAGE minigel (GenScript USA Inc) was loaded with 20 μg protein for each sample and run in MOPS buffer at 200V for 30 min. After electrophoresis, the SurePAGE minigel was stained with Commassie Blue for 30 min and washed for 12 h, followed with observation in a Bio-Rad gel imaging system.

2.3. Determination of the loading capacities of EGCG and NAC in BH-EGCG&NAC@MM

The freeze-dried BH-EGCG&NAC@MM (2 mg) were dispersed in triple-distilled H$_2$O (6 mL), followed by measuring the absorbance at 690 and 200 nm. The loading capacities of EGCG and NAC in the macrophage membrane-coated nanoparticles were calculated based on the calibration curve of the absorbance of BH-EGCG at 690 nm and NAC at 200 nm.

In detail, the loading capacity of BH-EGCG in BH-EGCG&NAC@MM was calculated according to the following equation:

$$\text{Loading capacity of BH} - \text{EGCG}\ (\%) = \frac{m_{\text{BH-EGCG}}}{m_{\text{BH-EGCG\&NAC@MM}}} \times 100\%$$

where $m_{\text{BH-EGCG}}$ is the mass of loaded BH-EGCG, $m_{\text{BH-EGCG\&NAC@MM}}$ is the mass of free-dried BH-EGCG&NAC@MM. The loading capacity of BH-EGCG in BH-EGCG&NAC@MM was determined as 54.4%, and thus the weight percentage of EGCG in BH-EGCG&NAC@MM could be calculated as 23.4%.

The loading capacity of NAC in BH-EGCG&NAC@MM was calculated according to the following equation:

$$\text{Loading capacity of NAC (\%)} = \frac{m_{\text{NAC}}}{m_{\text{BH-EGCG\&NAC@MM}}} \times 100\%$$

where m_{NAC} is the mass of loaded NAC, $m_{\text{BH-EGCG\&NAC@MM}}$ is the mass of free-dried BH-EGCG&NAC@MM. The loading capacity of NAC in BH-EGCG&NAC@MM was determined as 7.6%.

2.4. In vitro release profiles of EGCG and NAC

In vitro drug release profiles of EGCG from BH-EGCG, BH-EGCG@MM or BH-EGCG&NAC@MM were evaluated in PBS solution (pH 7.4) containing different concentrations of H_2O_2 as the release medium. Various nanoparticles (2 mL) were added into a dialysis bag (cut-off molecular weight: 500 Da), and then immersed into the release medium (50 mL) in triplicate and incubated in a shaking water bath with 100 rpm at 37 °C. At predetermined time intervals, the aliquots (2 mL) were taken out and the release medium was refilled to 50 mL with fresh release medium. The withdrawn aliquots were sampled and analyzed for EGCG content through the absorption-based calibration curve at 275 nm. For in vitro drug release profiles of NAC from BH-EGCG&NAC@MM, the withdrawn aliquots were sampled and analyzed for NAC content through the absorption-based calibration curve at 200 nm.

In detail, the EGCG or NAC content in the withdrawn aliquots of BH-EGCG&NAC@MM were calculated according to the following equation set:

$$A_{275} = \varepsilon_{\text{EGCG(275)}} \times c_{\text{EGCG}} \times L + \varepsilon_{\text{NAC(275)}} \times c_{\text{NAC}} \times L$$

$$A_{200} = \varepsilon_{\text{EGCG(200)}} \times c_{\text{EGCG}} \times L + \varepsilon_{\text{NAC(200)}} \times c_{\text{NAC}} \times L$$

where A_{275} and A_{200} are the absorbance of BH-EGCG&NAC@MM at 275 nm and 200 nm, respectively; $\varepsilon_{\text{EGCG(275)}}$ and $\varepsilon_{\text{EGCG(200)}}$ are the mass extinction coefficients of EGCG at 275 nm and 200 nm respectively; $\varepsilon_{\text{NAC(275)}}$ and $\varepsilon_{\text{NAC(200)}}$ are the mass extinction coefficients of NAC at 275 nm and 200 nm respectively; c_{EGCG} and c_{NAC} are mass concentrations of EGCG and NAC, respectively; L is 1 cm, representing the optical path length. The mass extinction coefficients were determined by the Beer-Lambert Law.

2.5. Concanavalin A (Con A)-induced autoimmune hepatitis (AIH) mouse model

For diagnosis purpose, to establish the AIH model, the mice were intravenously (i.v.) injected with a single dose of ConA (15 mg kg^{-1} in 200 μL saline) as the model group. Additionally, a group of healthy mice was used as the control group.

For therapy purpose, after being i.v. injected with Con A (15 mg kg^{-1} in 200 μL saline), the mice were subjected to treatment with different formulations via intravenous injection. The mice were randomly divided into 6 groups (n = 7 for each group) as follows: G1: Healthy mice without Con A administration. G2: The model mice receiving therapy with saline (200 μL) at 6, 12, 24, 30, 48, 54, 72, 78 h. G3: The model mice receiving therapy with free EGCG (2.5 mg kg^{-1}) at 6, 12, 24, 30, 48, 54, 72, 78 h. G4: The model mice receiving therapy with free NAC (0.75 mg kg^{-1}) at 6, 12, 24, 30, 48, 54, 72, 78 h. G5: The model mice receiving therapy with the mixture of BH-EGCG (5.8 mg kg^{-1}) and NAC (0.75 mg kg^{-1}) at 6, 12, 24, 30, 48, 54, 72, 78 h. G6: The model mice receiving therapy with BH-EGCG&NAC@MM (10 mg kg^{-1}) at 6, 12, 24, 30, 48, 54, 72, 78 h. The freeze-dried BH-EGCG and BH-EGCG&NAC@MM were reconstituted (re-dispersed) in saline for utilization in the therapy experiments.

2.6. Carrageenan (CAR)-induced hind paw edema mouse model

For diagnosis purpose, the mice were subcutaneously (s.c.) injected with CAR (20 mg kg^{-1} in 50 μL saline) in the plantar region of the right hind paws as the model group. Additionally, a group of healthy mice were s.c. injected with saline (50 μL) in the plantar region of the right hind paws and used as the control group.

For therapy purpose, after being s.c. injected with CAR, the mice were subjected to treatment with different formulations via intravenous injection. The mice were randomly divided into 6 groups (n = 7 for each group) as follows: G1: Healthy mice without CAR administration. G2: The model mice receiving therapy with saline (200 μL) at 2, 8, 14, 26, 32, 38 h. G3: The model mice receiving therapy with free EGCG (2.5 mg kg^{-1}) at 2, 8, 14, 26, 32, 38 h. G4: The model mice receiving therapy with free NAC (0.75 mg kg^{-1}) at 2, 8, 14, 26, 32, 38 h. G5: The model mice receiving therapy with the mixture of BH-EGCG (5.8 mg kg^{-1}) and NAC (0.75 mg kg^{-1}) at 2, 8, 14, 26, 32, 38 h. G6: The model mice receiving therapy with BH-EGCG&NAC@MM (10 mg kg^{-1}) at 2, 8, 14, 26, 32, 38 h. The freeze-dried BH-EGCG and BH-EGCG&NAC@MM were reconstituted (re-dispersed) in saline for utilization in the therapy experiments.

2.7. In vivo imaging for ConA-induced AIH model mice

The near-infrared (NIR) fluorescent imaging was conducted on Ami small animal imaging system from Spectral Instruments Imaging and the optoacoustic (OA) imaging (MSOT imaging) was conducted on inVision128 MSOT system from iThera Medical GmbH. Mice were depilated with commercial depilatory cream before the imaging experiments. The freeze-dried BH-EGCG and BH-EGCG&NAC@MM were reconstituted (re-dispersed) in saline for utilization in the imaging experiments.

For the purpose of detection and diagnosis, mice were subjected to imaging experiments at 4 h after the model establishment. Mice were i.v. injected with BH-EGCG or BH-EGCG&NAC@MM (equivalent dosage of 5 mg kg^{-1} BH-EGCG in two formulations) and imaged at predetermined time intervals (including 0, 5, 10, 20, 30, 40, 50 and 60 min). The NIR fluorescent imaging was conducted with the excitation filter of 675 nm and the emission filter of 730 nm. In MSOT imaging, 680, 695, 700, 715, 730, 760, 780, 800 and 850 nm were selected considering the major absorbance turning points of BH–OH, Hb, and HbO$_2$, and 10 frames per wavelength were obtained. Among them, 850 nm was chosen as the background wavelength to reflect the anatomy of mice. Cross-sectional images were acquired through scanning the mice body covering the trunk from the liver to the hind legs with a step size of 0.5 mm. Afterwards, the two-dimensional (2D) cross-sectional images were reconstructed to create the z-stack orthogonal-view three-dimensional (3D) images. Spectral unmixing was utilized to separate signals contributed by BH–OH and other different photoabsorbers such as hemoglobin.

For the purpose of monitoring therapeutic efficacy, mice from different groups (named as G1-G6, see "*Section 2.5*" for the details of the mice's grouping) were i.v. injected with BH-EGCG&NAC@MM (equivalent dosage of 5 mg kg^{-1} BH-EGCG) at 44 h (received 4 therapeutic injections) and 92 h (received 8 therapeutic injections) after the model establishment. Then, the mice were subjected to imaging experiments at 30 min after the nanoparticles' i.v. injection. The NIR fluorescent imaging was conducted with the excitation filter of 675 nm and the emission filter of 730 nm. In MSOT imaging, 680, 695, 700, 715, 730, 760, 780, 800 and 850 nm were selected considering the major absorbance turning points of BH–OH, Hb, and HbO$_2$, and 10 frames per wavelength were obtained. Among them, 850 nm was chosen as the background wavelength to reflect the anatomy of mice. Cross-sectional images were acquired through scanning the mice body covering the trunk from the liver to the hind legs with a step size of 0.5 mm. Afterwards, the two-dimensional (2D) cross-sectional images were reconstructed to create the z-stack orthogonal-view three-dimensional (3D) images. Spectral unmixing was utilized to separate signals contributed
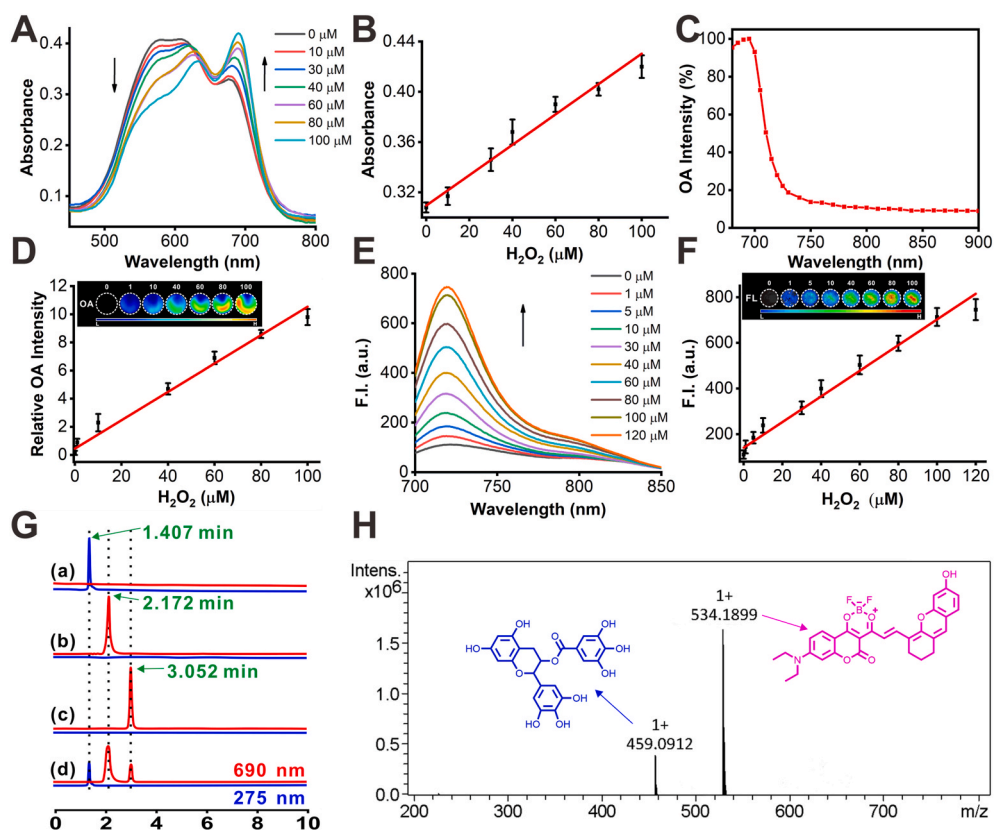
Fig. 2. Response mechanism of BH-EGCG towards H_2O_2. (A) Absorption spectra for BH-EGCG (10 μM) upon reaction with different concentrations of H_2O_2 in PBS solution (pH 7.4, containing 5% DMSO) for 20 min. (B) The relationship between the absorbance at 690 nm with the concentrations of H_2O_2 corresponding to (A). (C) The wavelength-dependence optoacoustic (OA) intensity (%) spectrum of BH-EGCG upon reaction with H_2O_2 (100 μM) for 20 min. (D) The relationship between the relative OA intensity at 690 nm with the concentrations of H_2O_2. The inset shows the phantom images of reaction solution at 690 nm in the presence of varied concentrations of H_2O_2 acquired from MSOT system. (E) Fluorescence spectra for BH-EGCG (10 μM) upon reaction with different concentrations of H_2O_2 in PBS solution (pH 7.4, containing 5% DMSO) for 20 min. Excitation: 675 nm. (F) The relationship between the fluorescent intensity at 720 nm with the concentrations of H_2O_2 corresponding to (E). The inset shows the representative images of reaction solution in the presence of varied concentrations of H_2O_2 acquired from AMI imaging system (excitation filter: 675 nm; emission filter: 730 nm). (G) HPLC chromatograms for (a) EGCG, (b) BH–OH, (c) BH-EGCG, and (d) BH-EGCG treated with H_2O_2 (100 μM) for 10 min. The mobile phase is methanol and the flow rate is 1.0 mL min^{-1}. Red lines represent signal acquired at 690 nm; Blue lines represent signal acquired at 275 nm. (H) HR Mass spectrum of BH-EGCG (10 μM, in pH 7.4 PBS containing 5% DMSO) after being reacted with H_2O_2 (80 μM) for 30 min.

(For interpretation of the references to colour in this figure legend, the reader is referred to the Web version of this article.)

by BH–OH and other different photoabsorbers such as hemoglobin.

2.8. In vivo imaging for CAR-induced hind paw edema model mice

For the purpose of detection and diagnosis, the mice were subjected to imaging experiments at 4 h after the model establishment. On one hand, the model group mice were s.c. injected with BH-EGCG&NAC@MM in the plantar region of the right hind paws and imaged at predetermined time intervals (including 0, 5, 10, 15, 20 and 25 min) by NIR fluorescent imaging and MSOT imaging. On the other hand, the mice from different groups (the healthy mice or the model mice) were i.v. injected with BH-EGCG or BH-EGCG&NAC@MM (equivalent dosage of 5 mg kg^{-1} BH-EGCG in two formulations) and imaged at predetermined time intervals (including 0 min, 20 min, 40 min, 60 min, 80 min, 2 h, 6 h, and 24 h) by NIR fluorescent imaging. The NIR fluorescent imaging was conducted with the excitation filter of 675 nm and the emission filter of 730 nm. In MSOT imaging, 680, 695, 700, 715, 730, 760, 780, 800 and 850 nm were selected as the major absorbance turning points of BH–OH, Hb, and HbO$_2$, and 10 frames per wavelength were obtained. Among them, 850 nm was chosen as the background wavelength to reflect the anatomy of mice. Cross-sectional images were acquired through scanning the mice body covering the trunk from the liver to the hind legs with a step size of 0.5 mm. Afterwards, the two-dimensional (2D) cross-sectional images were reconstructed to create the z-stack orthogonal-view three-dimensional (3D) images. Most importantly, spectral unmixing was utilized to separate signals contributed by BH–OH and other different photoabsorbers such as hemoglobin.

For the purpose of monitoring therapeutic efficacy, mice from different groups (named as G1-G6, see "*Section 2.6*" for the details of the mice's grouping) were i.v. injected with BH-EGCG&NAC@MM (equivalent dosage of 5 mg kg^{-1} BH-EGCG) at 72 h (received 6 therapeutic injections) after the model establishment. Then, the mice were subjected to NIR fluorescent imaging at 6 h after the nanoparticles' injection. The NIR fluorescent imaging was conducted with the excitation filter of 675 nm and the emission filter of 730 nm.

3. Results and discussions

3.1. Synthesis of the prodrug BH-EGCG and its spectral response toward H_2O_2

The ROS-responsive molecular prodrug BH-EGCG was synthesized according to the route presented in Schemes S1 and S2. The prodrug BH-EGCG was formed via the coupling between the NIR fluorophore (BH–BOH) with EGCG. The molecular structures of key intermediates and final product were characterized by ^{1}H NMR and HR-MS (Figs. S1–10). As shown in Fig. S8, there are four possible coupling modes between EGCG and BH–BOH, while two of them prevail as revealed by ^{1}H NMR spectra.

The phenylboronate is sensitive to reactive oxygen species such as H_2O_2 which can induce the scission of the carbon-boron bond [64,65], and thus the optical properties of BH-EGCG in the absence and presence of H_2O_2 were determined to investigate the ROS-responsive behavior of BH-EGCG. Fig. 2A and B and Fig. S11 show the effect of H_2O_2 on the absorption spectra of BH-EGCG. Clearly, incubation with H_2O_2 decreases the absorption at around 600 nm while increases the absorption at around 690 nm, and this change in absorption is enough to generate
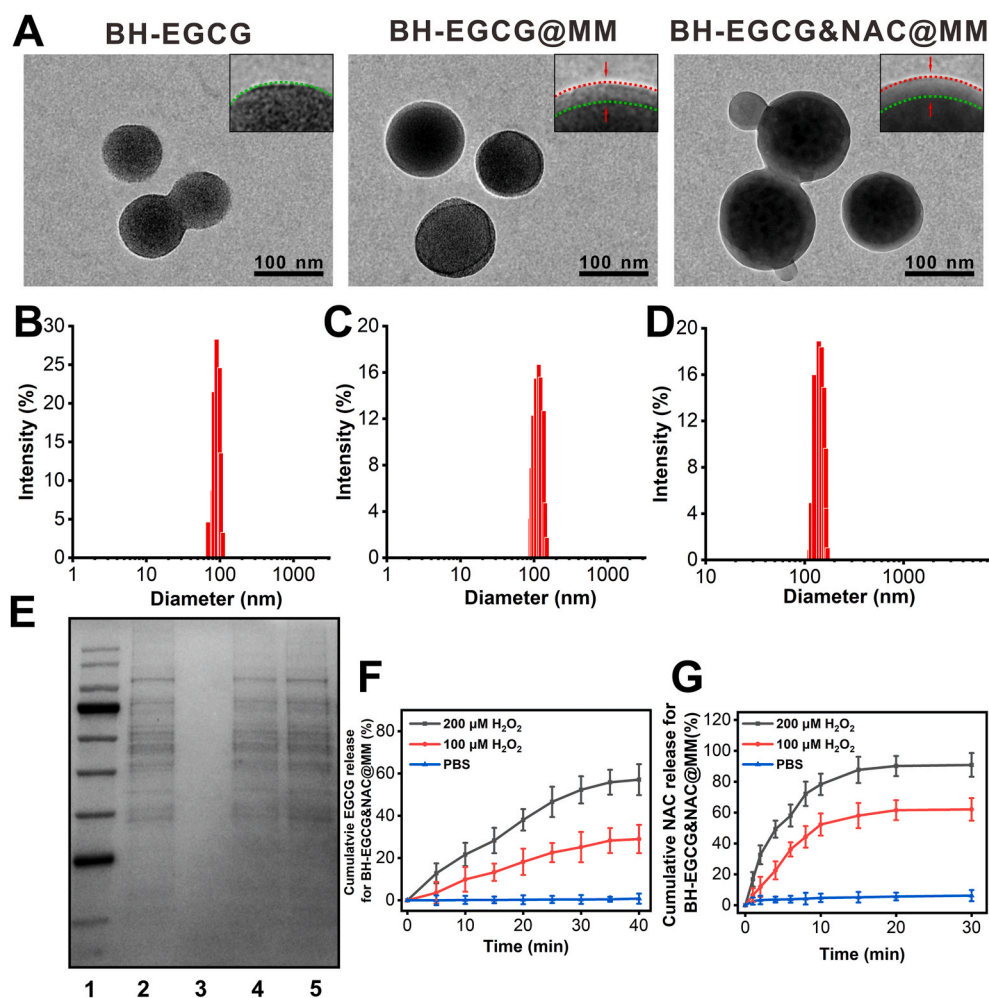
Fig. 3. Characterizations of nanosystems. (A) Typical TEM images of the three nanoparticles. Scale bar: 100 nm. Green dotted line and red dotted line indicate the edge of the nanoparticles and the boundaries of the coated cell membrane shells respectively. Size distribution obtained with dynamic light scattering (DLS) method for nanoparticles BH-EGCG (B), BH-EGCG@MM (C) and BH-EGCG&NAC@MM (D). (E) Protein profiles determined by SDS-PAGE electrophoresis assay. 1: protein marker; 2: pure MM; 3: BH-EGCG; 4: BH-EGCG@MM; 5: BH-EGCG&NAC@MM. In vitro cumulative release profiles of EGCG (F) or NAC (G) from the BH-EGCG&NAC@MM in PBS solution with varied concentration of H_2O_2 at varied time points. (For interpretation of the references to colour in this figure legend, the reader is referred to the Web version of this article.)

strong relative optoacoustic (OA) signal in the MSOT system through spectral unmixing process and equipment parameters optimization. As shown in Fig. 2C and D, the relative OA intensities at 690 nm increases significantly with the increasing H_2O_2 concentrations, demonstrating that the optoacoustic imaging can be utilized to monitor this ROS-mediated process. In addition, the fluorescence response of BH-EGCG toward H_2O_2 is shown in Fig. 2E, F and Fig. S12. The fluorescent intensity at 720 nm increases remarkably with the enhancing concentrations of H_2O_2. The detection limit of BH-EGCG towards H_2O_2 is determined as 0.34 μM (3 σ/slope with Fig. 2F). Moreover, BH-EGCG displays good selectivity and specificity toward H_2O_2 over various interferents, as shown in Figs. S13–14. In addition, the absorption and emission spectra of BH-EGCG after being incubated with H_2O_2 are similar to those of the synthesized BH–OH as illustrated in Figs. S15–16, connoting that after reaction with H_2O_2, BH-EGCG releases the chromophore BH–OH (the activated chromophore). What's more, high-performance liquid chromatography (HPLC) was also performed to substantiate the release of the parent drug EGCG from BH-EGCG upon being incubated with H_2O_2, as shown in Fig. 2G. Upon the incomplete reaction between BH-EGCG and H_2O_2, the characteristic peak of the BH-EGCG at 3.052 min decreases, and two new peaks at 1.407 min (corresponding to EGCG) and 2.172 min (corresponding to BH–OH) can be clearly noticeable. Mass spectrum (MS) was also conducted for additional verification (Fig. 2H). It is clearly overt that upon complete reaction between BH-EGCG and H_2O_2, two new peaks at $m/z = 459.0912$ (corresponding to $[EGCG + H]^+$) and $m/z = 534.1899$ (corresponding to $[BH–OH + H]^+$) emerge, which manifests the H_2O_2-induced transformation of BH-EGCG into EGCG and BH–OH. These results

corroborate that H_2O_2 cleaves the carbon-boron bonds in BH-EGCG and thereby releases the parent drug EGCG and in the meantime activates the chromophore for dual-mode (fluorescence and optoacoustic) imaging.

3.2. Preparation of the macrophage membrane coated nanoparticles BH-EGCG@MM and BH-EGCG&NAC@MM

Due to the coexistence of both hydrophilic and hydrophobic moieties in its molecular structure, in aqueous media BH-EGCG promptly forms nanoparticles. The obtained BH-EGCG nanoparticles were immediately subject to macrophage membrane coating by microstream extrusion [66–68]. The resultant nanoparticles were denoted as BH-EGCG@MM. Moreover, during the coating process, an antioxidant precursor and ROS scavenger N-acetyl cysteine (NAC) was also loaded into the nanoparticles to form a nanodrug system (BH-EGCG&NAC@MM). Transmission electron microscopy (TEM) observation and DLS measurement for the nanoparticles were carried out to authenticate the successful coating of cell membrane on BH-EGCG cores. The morphologies of the three kinds of nanoparticles (BH-EGCG, BH-EGCG@MM and BH-EGCG&NAC@MM, the three kinds of nanoparticles were prepared separately) were observed on TEM. As shown in Fig. 3A–D, both BH-EGCG@MM and BH-EGCG&NAC@MM exhibit spherical core-shell structure; and upon membrane coating, the mean diameter of the nanoparticles increases from 80 to 100 nm for BH-EGCG to 100–120 nm for BH-EGCG@MM, implying the coating of cell membrane on the surface of particles [66,67]. With NAC loaded into the membrane-coated nanoparticles, the mean particle size further increases to 120–140 nm,
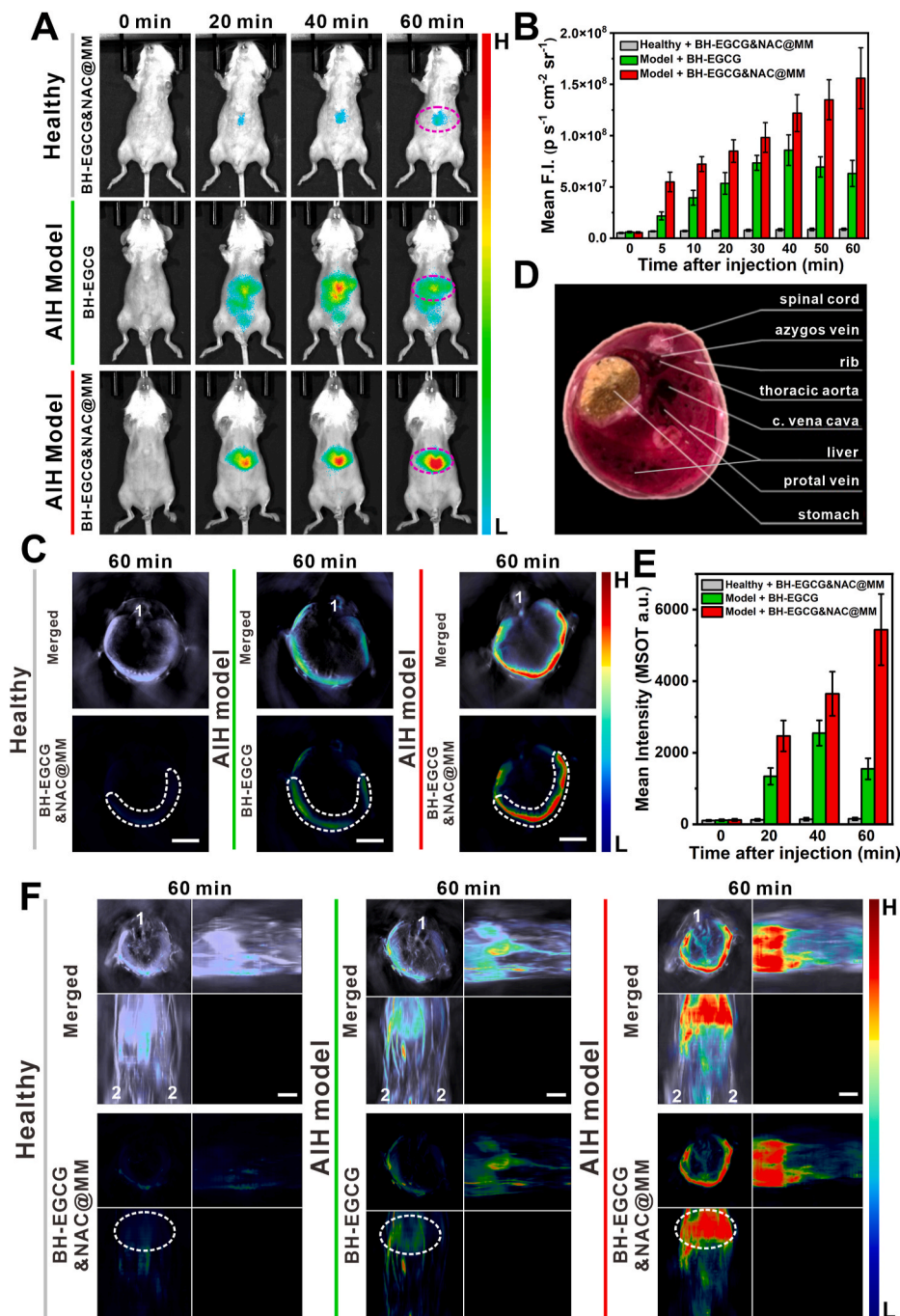
Fig. 4. Diagnostic applications of BH-EGCG&NAC@MM in ConA-induced AIH mouse model. (A) NIR fluorescence images for the healthy mice injected (i.v.) with BH-EGCG&NAC@MM and the AIH model mice injected (i.v.) with BH-EGCG or BH-EGCG&NAC@MM at designated time intervals. The mice were in supine posture. Magenta dotted circle represents the ROI covering the whole liver. Excitation filter: 675 nm, emission filter: 730 nm. (B) Mean fluorescence intensities covering the liver (the ROI) of the mice in (A) at designated time intervals (n = 7). (C) Cross-sectional MSOT images for the healthy mice injected (i.v.) with BH-EGCG&NAC@MM and the AIH model mice injected (i.v.) with BH-EGCG or BH-EGCG&NAC@MM at 60 min after the nanoparticles' injection. Upper row: Merged signals from the activated chromophore with the background at 850 nm; Lower row: Un-mixing signal from the activated chromophore. "1" indicates spinal cord. The mice were in prone posture. White dotted circle shows the ROI covering the liver. Scale bar: 6 mm. (D) A cryosection image of male mouse matching cross section shown in (C). (E) Mean OA intensities of the ROI in the healthy mice injected (i.v.) with BH-EGCG&NAC@MM and the AIH model mice injected (i.v.) with BH-EGCG or BH-EGCG&NAC@MM at designated time intervals (n = 7). (F) Orthogonal-view 3D (MIP) images for the healthy mice injected (i.v.) with BH-EGCG&NAC@MM and the AIH model mice injected (i.v.) with BH-EGCG or BH-EGCG&NAC@MM at 60 min after nanoparticles' injection (the scanning region is indicated in Fig. S28A). Upper row: Merged signals from the activated chromophore with the background at 850 nm; Lower row: Un-mixing signal from the activated chromophore. The mice were in prone posture. "1" indicates spinal cord. "2" indicates hind limbs. White dotted circle shows the ROI covering the whole liver. Scale bar: 6 mm.

as NAC has rich proton-donating and proton-accepting moieties which might lead to interactions with BH-EGCG (e.g., hydrogen bonding interactions) and thus loosely-packed structures might form in BH-EGCG&NAC@MM. Moreover, the protein profiles for pure macrophage membrane and the three kinds of nanoparticles were determined by SDS-PAGE electrophoresis. As shown in Fig. 3E, the protein compositions in macrophage membrane are mostly retained in the macrophage membrane coated nanoparticles (BH-EGCG@MM and BH-EGCG&NAC@MM), but not found in BH-EGCG. The results further validate the successful coating of cell membrane on nanoparticles, which could endow the nanoparticles the capability to target inflammatory tissue for diagnostic bioimaging and therapeutic drug delivery. In addition, the zeta potentials were also measured to further verify the successful coating of MM for the particles (Fig. S17). It can be seen that

the zeta potential for BH-EGCG is ~ -17 mV, while the zeta potentials for BH-EGCG@MM and BH-EGCG&NAC@MM are ~ -30 mV. The MM-coated nanosystems' zeta potentials are close to the pure MM's zeta potential. Additionally, as shown in Fig. S18, the mean diameter of the MM-coated nanosystem is hardly changed over a span of 48 h in PBS or PBS containing 50% FBS, indicating the relatively high stability of the nanoparticles [67].

The drug loading of EGCG and NAC in the nanodrug BH-EGCG&NAC@MM were determined as 23.4% and 7.6% respectively by absorption spectrometry according to the predetermined calibration curves of EGCG and NAC shown in Fig. S19. The in vitro H_2O_2-mediated EGCG release from the two nanosized formulations (BH-EGCG and BH-EGCG@MM) were also determined via absorption spectrometry in PBS solutions in the presence of varied concentrations of H_2O_2 at varied time

points. As shown in Fig. S20, both the two formulations exhibit moderate drug release rates of EGCG in the presence of H_2O_2. At 200 μM of H_2O_2, they display a relatively high accumulative drug release rate up to ~60% upon incubation for 40 min, whereas almost no EGCG release is observed in the absence of H_2O_2, implying H_2O_2 plays crucial role in EGCG release. Notably, the EGCG release rate from BH-EGCG@MM was found rather close to that from BH-EGCG under the same condition (Fig. S20), suggesting that the macrophage membrane (MM) coating does not significantly affect the response of the nanodrugs toward H_2O_2. Similarly, the accumulative release rates of EGCG or NAC from BH-EGCG&NAC@MM were also determined (Fig. 3F and G). The release rate of NAC reaches ~90% at 20 min upon incubation with 200 μM of H_2O_2, while that of EGCG reaches ~60% at 40 min. NAC displays faster release rate than EGCG, which could be due to the hydrophilic feature of NAC as well as the fact that EGCG is covalently coupled to the chromophore. These results proved that the two drugs, including NAC and EGCG, can be released in the presence of H_2O_2 in vitro.

3.3. BH-EGCG&NAC@MM for targeting and detecting inflammatory diseases in mouse models with NIR fluorescence and MSOT imaging

Before in vivo imaging, the cytotoxicity of BH-EGCG&NAC@MM was evaluated using RAW264.7 by MTT assay, as displayed in Fig. S21. The viabilities of RAW264.7 cells maintained over 88% upon incubation with relatively high concentrations of BH-EGCG&NAC@MM (up to 300 mg L^{-1}), revealing the low cytotoxicity of the nanosystem. In addition, we evaluated the biosafety of BH-EGCG&NAC@MM by intravenously injecting BH-EGCG&NAC@MM (10 mg kg^{-1}, in 200 μL saline) or saline (200 μL, as the control) into two groups of healthy mice. As shown in Fig. S22, at 24 h after the i.v. injection of BH-EGCG&NAC@MM, there is little histopathological difference between the major organs' sections (H&E staining) garnered from the two groups of mice, manifesting that BH-EGCG&NAC@MM is of good biosafety. Moreover, the activated probe (BH–OH) and the MM-coated nanoparticle loaded with BH–OH (BH–OH@MM) were employed for evaluating the pharmacokinetics of the nanosystem. Blood samples were harvested at various time points after the intravenous injection of BH–OH or BH–OH@MM for fluorescence measurement (excitation filter: 675 nm, emission filter: 730 nm), and the results are displayed in Fig. S23. It can be seen that the coating of MM enhances the blood retention.

Afterwards, we first employed autoimmune hepatitis (AIH) mouse model to investigate BH-EGCG&NAC@MM's capability to detect inflammatory disease. For this purpose, the concanavalin A (ConA)-induced AIH mouse model was established [69–71]. To validate the successful establishment of the AIH mouse model, histological analysis (H&E staining) and blood biochemical tests were conducted. The histological images of the liver sections (H&E staining) from the healthy mice treated with saline and the AIH model mice induced by ConA are shown in Fig. S24, and it is indubitable that the liver sections of the control (healthy mice) display normal morphology. In contrast, in the liver sections of the AIH model mice, there exist obvious necrosis and portal inflammatory infiltration, implying liver damages caused by ConA. Serum alanine aminotransferase (ALT) is an enzyme crucial for identifying liver toxicity or liver damage [71,72], and the measured serum ALT levels are shown in Fig. S25. It is readily apparent that the ALT levels of the AIH model mice are much higher than the control group (healthy mice treated with saline), which further corroborates the liver damages caused by ConA and the successful establishment of the AIH mouse model. To evaluate the imaging and diagnostic capability of BH-EGCG&NAC@MM for AIH in mouse model through responding to the overexpressed ROS in inflammatory liver, we conducted NIR fluorescent imaging and MSOT imaging by intravenously injecting BH-EGCG or BH-EGCG&NAC@MM into the AIH model mice and the healthy mice. The mice in control group (healthy mice) were injected (i. v.) with BH-EGCG&NAC@MM, while the AIH model mice were injected (i.v.) with BH-EGCG or BH-EGCG&NAC@MM. Afterwards, the mice

were subjected to fluorescent imaging, and the imaging results are shown in Fig. 4A, and Fig. S26. It is readily observable that, the fluorescent signal in the healthy mice's liver region is much weaker than that of the AIH model mice, which is due to the fact that the ROS level in healthy liver is much lower than that in the inflammatory liver of the AIH model mice [43,73]. As depicted in Fig. 4A, the fluorescence signal of the AIH model mice progressively enhances in the liver region with the signal remaining quite evident at 60 min after BH-EGCG&NAC@MM's i.v. injection, and the fluorescence signal is much more salient compared to the AIH model mice i.v. injected with BH-EGCG or the healthy mice i.v. injected with BH-EGCG&NAC@MM. For the AIH model mice i.v. injected with BH-EGCG, the diffusion of fluorescence signal to the intestinal area is clearly observable at 20 min, and the strongest signal appears at 40 min. However, for the AIH model mice i.v. injected with BH-EGCG&NAC@MM, the fluorescence signal enhanced steadily within 60 min without diffusion to the intestinal area. In addition, the mean fluorescent intensities covering the liver (for the region of interest, ROI) in all groups at designated time points were recorded and given in Fig. 4B. These results demonstrate that the macrophage cell membrane coated on the particle's surface (BH-EGCG&NAC@MM) improves the accumulation of the nanoparticles in the inflammatory microenvironment of AIH due to their inflammation-chemotactic nature.

Since multispectral optoacoustic tomography (MSOT) imaging system can generate cross-sectional 2D images using tomography technique and render a stack of 2D images into orthogonal-view 3D images, which are conducive to providing 3D information of disease site [57–63]. To accurately locate the AIH site and estimate the size of the disease site in mice, we performed MSOT imaging and presented the results in Fig. 4C–F and Figs. S27–28. The healthy mice were injected (i.v.) with BH-EGCG&NAC@MM, and the AIH model mice were injected (i.v.) with BH-EGCG or BH-EGCG&NAC@MM. The MSOT images for a typical cross-section at the liver region for AIH model mice are shown in Fig. 4C and Figs. S27 and a cryosection image (from the built-in images of the MSOT system) of a male mouse corresponding to this cross section is displayed in Fig. 4D, which shows the locations of organs. From Fig. 4C and Fig. S27, it is easily noticeable that only weak MSOT signals exist in the liver region of the healthy mice after being i.v. injected with the BH-EGCG&NAC@MM; while for the AIH model mice after being i.v. injected with BH-EGCG or BH-EGCG&NAC@MM, there are apparent signals in the liver regions, and the signals are much more evident for the AIH model mice injected (i.v.) with BH-EGCG&NAC@MM than the AIH model mice injected (i.v.) with BH-EGCG, revealing BH-EGCG&NAC@MM accumulate more in the inflamed liver where excessive ROS can activate the nanoparticles to give out optoacoustic signals. The mean optoacoustic intensities covering the liver region (ROI) of the mice in all groups at the designated time intervals displayed in Fig. 4E support this observation. Moreover, upon injection (i.v.) of the nanoparticles, the mice body from the liver to hind legs (as shown in Fig. S28) of different groups were subjected to tomographic imaging, and the obtained tomographic images were subsequently rendered as 3D orthogonal-view images, which are shown in Fig. 4F and Fig. S28. These 3D images display similar result as the cross-sectional MSOT images, for the healthy mice injected (i.v.) with BH-EGCG&NAC@MM only weak signals exist in the liver region, for the AIH model mice injected (i.v.) with BH-EGCG or BH-EGCG&NAC@MM noticeable signals appear in the liver regions, and the signals in the liver region of the AIH model mice injected (i.v.) with BH-EGCG&NAC@MM are much more pronounced than those of the AIH model mice injected (i.v.) with BH-EGCG. These results again validate that the nanoparticles coated with macrophage membrane (BH-EGCG&NAC@MM) can accumulate more efficiently in the inflammatory disease site and the in-situ ROS activates the nanoparticles and thereby giving out evident optoacoustic signals.

To further validate the above in vivo imaging results, the ex vivo imaging was conducted for the major organs garnered from different groups, as shown in Fig. S29. The organs were dissected at 60 min after
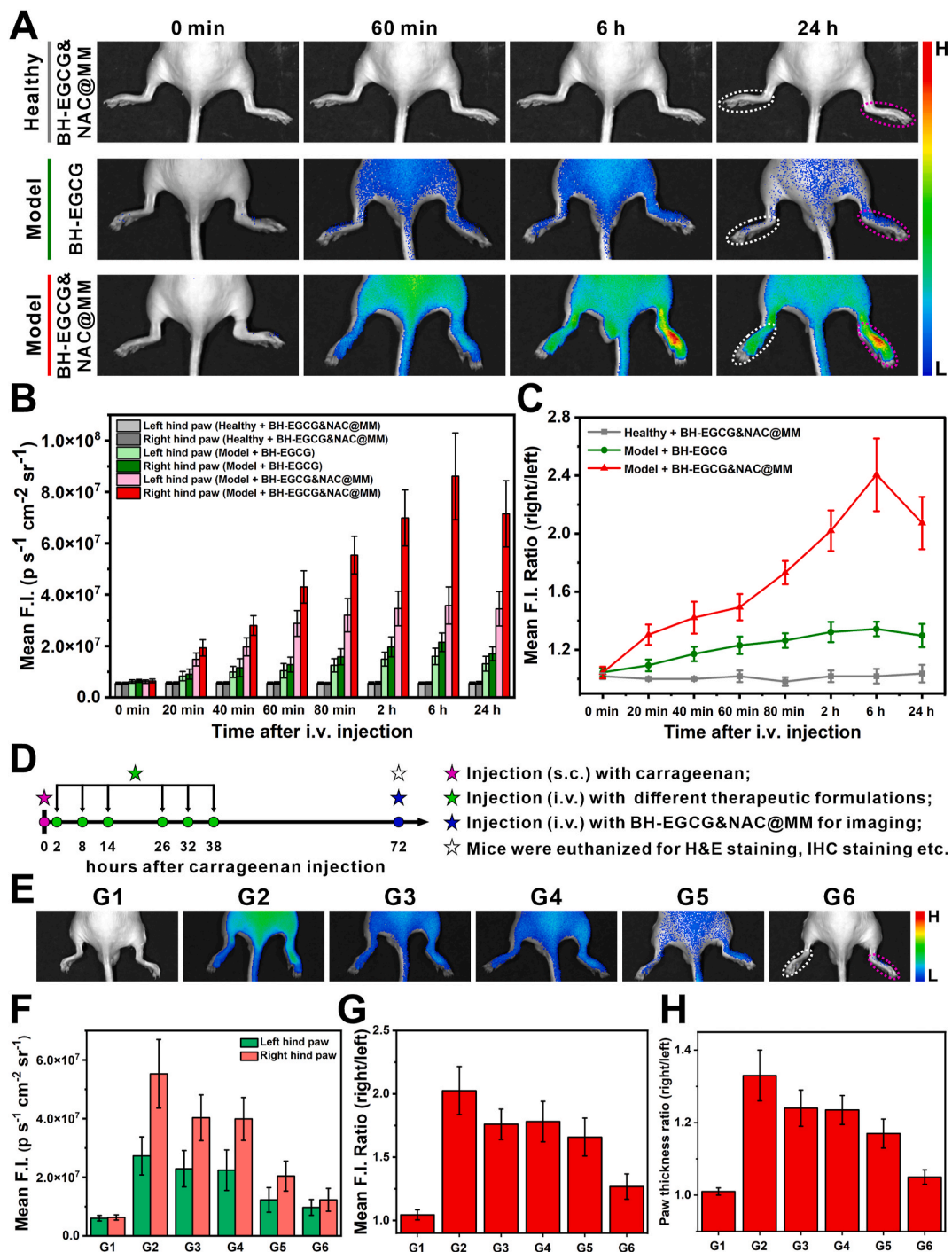
Fig. 5. Theranostic applications of BH-EGCG&NAC@MM in CAR-induced hind paw edema mouse model. (A) Fluorescence images for the healthy mice injected (i.v.) with BH-EGCG&NAC@MM and the CAR-induced hind paw edema model mice injected (i.v.) with BH-EGCG or BH-EGCG&NAC@MM at designated time intervals. The mice were subjected to imaging experiments at 4 h after the establishment of CAR-induced hind paw edema model. Magenta dotted circle displays the ROI covering the whole right hind paw. White dotted circle displays the ROI covering the whole left hind paw. The mice were in prone posture. Excitation filter: 675 nm; Emission filter: 730 nm. (B) Mean fluorescence intensities for the ROI covering the hind paws of mice in (A) at designated time intervals (n = 7). (C) The ratio of the fluorescence intensities for the ROI of right hind paw to left hind paw from the mice in (A) at designated time intervals (n = 7). (D) Experimental outline for treatment course of CAR-induced hind paw edema model. (E) Representative NIR fluorescent images for the mice from G1-G6 at 6 h after the injection (i.v.) of BH-EGCG&NAC@MM. The mice were subjected to imaging experiments at 72 h (received 6 therapeutic injections) after the establishment of CAR-induced hind paw edema mouse model. Magenta dotted circle displays the ROI covering the whole right hind paw. White dotted circle displays the ROI covering the whole left hind paw. The mice were in prone posture. Excitation filter: 675 nm; Emission filter: 730 nm. (F) Mean fluorescence intensities of the hind paws corresponding to the mice in (E) (n = 7). (G) The ratio of the fluorescence intensities for the ROI of right hind paw to left hind paw from the mice in (E) (n = 7). (H) The ratio of right paw thickness to left paw thickness corresponding to the mice in (E) (n = 7). (G1: Healthy mice without CAR administration. G2: The model mice receiving therapy with saline (200 μL) at 2, 8, 14, 26, 32, 38 h. G3: The model mice receiving therapy with free EGCG (2.5 mg kg^{-1}) at 2, 8, 14, 26, 32, 38 h. G4: The model mice receiving therapy with free NAC (0.75 mg kg^{-1}) at 2, 8, 14, 26, 32, 38 h. G5: The model mice receiving therapy with the mixture of BH-EGCG (5.8 mg kg^{-1}) and NAC (0.75 mg kg^{-1}) at 2, 8, 14, 26, 32, 38 h. G6: The model mice receiving therapy with BH-EGCG&NAC@MM (10 mg kg^{-1}) at 2, 8, 14, 26, 32, 38 h.)

the nanoparticles' injection. It is apodictic that the fluorescent or optoacoustic signals are concentrated in the livers from all three groups of mice, and almost no signals are observable in other organs. The weak signals in the liver of the healthy mice injected (i.v.) with BH-EGCG&NAC@MM might be due to the fact that only a slight amount of ROS exists endogenously in healthy mice's liver [43,73]. The signals in the liver of the AIH model mice injected (i.v.) with BH-EGCG&NAC@MM are stronger than the AIH model mice injected (i. v.) with BH-EGCG or the healthy mice injected (i.v.) with BH-EGCG&NAC@MM, this is because the over-expressed ROS such as H_2O_2 in the inflamed liver activates the nanoparticles and consequently turns on the fluorescent and optoacoustic signals. These ex vivo imaging data substantiate the above in vivo imaging results.

The imaging results manifest that BH-EGCG&NAC@MM can efficiently accumulate in the inflamed liver region and give out fluorescent and optoacoustic signals via responding to the in-situ biomarker H_2O_2 for the fluorescent/optoacoustic dual-mode imaging, and thus the macrophage membrane coated nanoparticle (BH-EGCG&NAC@MM) could act as a promisingly viable tool for targeting and diagnosing inflammation diseases through response to in-situ biomarker.

To further confirm BH-EGCG&NAC@MM's capability to target and image the inflammatory site, we employed BH-EGCG&NAC@MM in the carrageenan (CAR)-induced paw edema mouse model. The mouse model of CAR-induced paw edema has frequently been used as acute inflammation model and a convenient method for evaluating inflammatory response, as CAR is a well-studied chemical which stimulates the release of inflammatory mediators, including reactive oxygen species (ROS), reactive nitrogen species (RNS) and histamine [74–76]. To establish the right hind paw edema mouse model, CAR was subcutaneously injected into the plantar region of the right hind paw and the mice were subjected to imaging experiments at 4 h after the CAR's injection. The photographs of the healthy and the CAR-induced hind paw edema mice are shown in Fig. S30, it is clearly apparent that the right hind paw injected with CAR is obviously much swollen than the right hind paw of the healthy mouse. In addition, the tissue section (H&E staining) analysis was carried out for the basal layer of the right hind paw (Fig. S31), and obvious cartilage destruction and inflammatory infiltration can be observed in the basal layer of the right hind paw from the mice injected with CAR. These results confirm the successful establishment of the hind paw edema mouse model.

To confirm the responsiveness of BH-EGCG&NAC@MM toward ROS in inflammatory tissues, BH-EGCG&NAC@MM were first injected subcutaneously into the right hind paws of the CAR-induced hind paw edema model mice, and then NIR fluorescent imaging and MSOT imaging were conducted. The fluorescent imaging results are displayed in Fig. S32. It is readily seen that the NIR fluorescent signals in right hind paw enhances obviously after the nanoparticles' injection. Additionally, the mean fluorescence intensities of the ROI covering the whole right hind paw regions of the mice at designated time intervals are presented in Fig. S33. The 3D MSOT imaging results are displayed in Fig. S34. The scanning region in MSOT imaging covering the hind paws is shown in Fig. S34A. The 3D MSOT images also show that the optoacoustic signals in right hind paw increases obviously after the nanoparticles' injection (Fig. S34B). This is because the excessively expressed ROS (including H_2O_2) in the inflammatory tissues induced by CAR activates the nanoparticles and thus generates the fluorescent or optoacoustic signals.

Afterwards, the healthy mice were injected intravenously (i.v.) with BH-EGCG&NAC@MM, and the CAR-induced hind paw edema model mice were injected (i.v.) with BH-EGCG or BH-EGCG&NAC@MM, and then the mice were subjected to NIR fluorescent imaging. The imaging results are shown in Fig. 5A and Figs. S35–36. It is overt that no noticeable NIR fluorescent signal can be found in both the left and right hind paws of the healthy mice after injected (i.v.) with BH-EGCG&NAC@MM. While in the CAR-induced hind paw edema mice, the fluorescent signals in the swollen right hind paws are more evident than those in the left hind paws, in particular for the model mice injected (i.

v.) with BH-EGCG&NAC@MM, the fluorescent signals in the right hind paws are much stronger compared to those mice injected (i.v.) with BH-EGCG. These results corroborate that the macrophage-membrane coated nanoparticles (BH-EGCG&NAC@MM) are indeed more likely to accumulate in the inflammatory disease foci (the inflamed right hind paw in this case). The mean fluorescent intensities of the left and right hind paws in different groups of mice are given in Fig. 5B and the ratios of the right/left hind paw are given in Fig. 5C. It is lucid that, in CAR-induced hind paw edema model mice injected (i.v.) with BH-EGCG&NAC@MM, the fluorescence signal in right hind paw is the strongest and the ratio of right/left paw reaches the highest level at 6 h after nanoparticles' injection. These diagnostic imaging application in CAR-induced hind paw edema mice model convinces us of the capability for the nanosystem BH-EGCG&NAC@MM to actively target inflammatory distal limb.

3.4. BH-EGCG&NAC@MM for treatment of inflammatory diseases and monitoring therapeutic effect

Encouraged by the above results that BH-EGCG&NAC@MM can target and detect inflammatory disease sites, we set out to further employ the nanosystem to treat the inflammatory diseases as well as monitor the therapeutic effects. In this study, first, BH-EGCG&NAC@MM was employed for treating the CAR-induced hind paw edema. The therapeutic process is shown in Fig. 5D. The mice were divided into 6 groups (named as G1-G6) and treated with different therapeutic formulations as follows: G1 was the heathy mice treated only with saline, G2 was the CAR-induced hind paw edema mice treated with saline, G3 was the CAR-induced hind paw edema model mice treated with free EGCG, G4 was the CAR-induced hind paw edema mice treated with free NAC, G5 was the CAR-induced hind paw edema model mice treated with BH-EGCG and free NAC, G6 was the CAR-induced hind paw edema model mice treated with BH-EGCG&NAC@MM. The dosage of EGCG at 2.5 mg kg^{-1} and NAC at 0.75 mg kg^{-1} were adopted for different therapeutic formulations in every single therapeutic injection. After 6 treatments, the mice of G1-G6 were i.v. injected with BH-EGCG&NAC@MM at 72 h post CAR injection, and subjected to NIR fluorescent imaging at 6 h post injection (i.v.) of BH-EGCG&NAC@MM, the fluorescence images were acquired and fluorescent intensities of the hind paws from G1-G6 were recorded as shown in Fig. 5E–G. It is readily observable that after treatment the fluorescent intensities for the right hind paws of G3, G4, G5 and G6 all decrease, and the intensity for the right hind paw of G6 is the weakest among them, and is closest to that of G1 (healthy mice). Thereafter, we also measured the dorsal plantar thickness at metatarsal level using a Vernier caliper to reflect the swelling severity, and the ratio of right paw thickness to left paw thickness (right/left) defined as the paw thickness index is shown in Fig. 5H. It is pellucid that the ratio of the paw thickness index shows the same pattern as that of fluorescent intensity ratios (Fig. 5G), proving that BH-EGCG&NAC@MM could be used to evaluate the efficacy of different therapeutic formulations. It is known that NAC has a short half-life which results in low delivery efficiency to the lesion site [77]. The ratio of fluorescent intensity in G6 is lower than that in G5, which reflects that the therapeutic efficacy of BH-EGCG&NAC@MM is better than that of the simple mixture of BH-EGCG and free NAC. The reason could be that the nanoparticles successfully deliver NAC to the inflamed right hind paw and the in-situ released NAC and EGCG for treatment leads to the improved therapeutic efficacy. In addition, to confirm the therapeutic effects from a different perspective, histological sections (H&E staining) and IHC analyses for IL-6 expression of the hind paw tissues from different groups were carried out, and the results are shown in Fig. S37. Compared to other treatment groups (G2-G5), G6 exhibits the lowest extent of cartilage destruction and inflammatory infiltration, which is closest to the situation in G1 and reflects the best therapeutic efficacy among the treatment groups. This result is in conformity with the results of fluorescence imaging. Furthermore, treatment with BH-EGCG&NAC@MM also leads to the reduced level of IL-6 (a
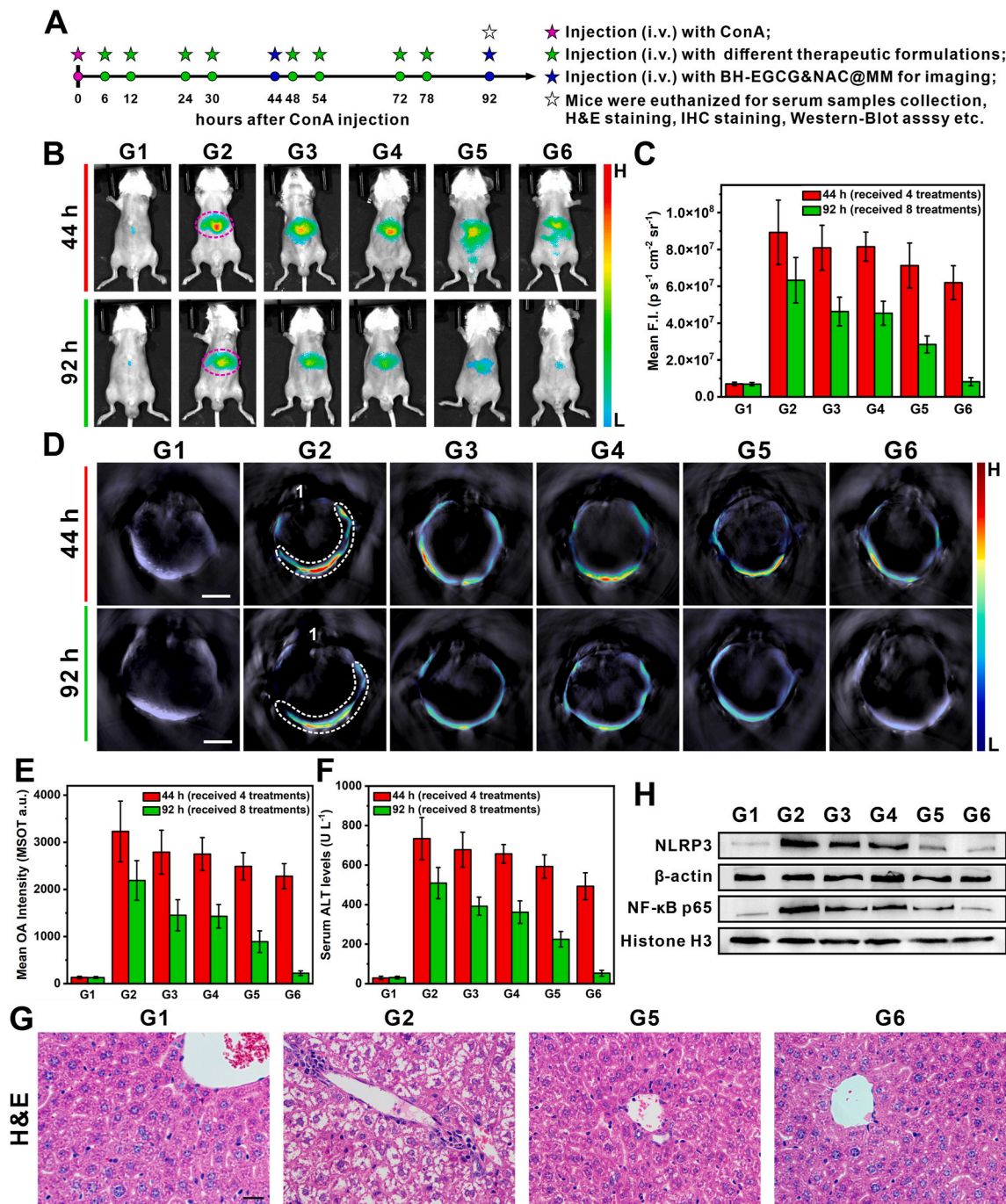
Fig. 6. Theranostic applications of BH-EGCG&NAC@MM in ConA-induced AIH mouse model. (A) Experimental outline for treatment course of ConA-induced AIH mice. (B) NIR fluorescent images of the mice from G1-G6 at 30 min post intravenous injection of BH-EGCG&NAC@MM after receiving 4 or 8 therapeutic injections. Magenta dotted circle displays the ROI covering the whole liver. The mice were in supine posture. Excitation filter: 675 nm; Emission filter: 730 nm. (C) Mean fluorescent intensities in the livers from the mice in G1-G6 at 30 min post intravenous injection of BH-EGCG&NAC@MM after receiving 4 or 8 therapeutic injections. (n = 7). (D) Cross-sectional MSOT images of the mice from G1-G6 at 30 min after intravenous injection of BH-EGCG&NAC@MM after receiving 4 or 8 therapeutic injections. The mice were in prone posture. "1" shows the spinal cord; White dotted circle displays the ROI covering the whole liver. Scale bar = 6 mm. (E) Mean optoacoustic intensities of the livers from G1-G6 groups at 30 min after intravenous injection of BH-EGCG&NAC@MM upon receiving 4 or 8 therapeutic injections. (F) Serum ALT levels of G1-G6 tested by ELISA kits (n = 7). (G) H&E staining of the liver sections from mice in G1, G2, G5 and G6 after receiving 8 therapeutic injections. (H) Western blot analyses for the cytoplasmic NLRP3 level and nuclear NF-κB level in liver tissues dissected from G1-G6. β-actin served as the loading control of cytosolic protein and Histones H3 as the loading control of nuclear protein. (G1: Healthy mice without Con A administration. G2: The model mice receiving therapy with saline (200 μL) at 6, 12, 24, 30, 48, 54, 72, 78 h. G3: The model mice receiving therapy with free EGCG (2.5 mg kg^{-1}) at 6, 12, 24, 30, 48, 54, 72, 78 h. G4: The model mice receiving therapy with free NAC (0.75 mg kg^{-1}) at 6, 12, 24, 30, 48, 54, 72, 78 h. G5: The model mice receiving therapy with the mixture of BH-EGCG (5.8 mg kg^{-1}) and NAC (0.75 mg kg^{-1}) at 6, 12, 24, 30, 48, 54, 72, 78 h. G6: The model mice receiving therapy with BH-EGCG&NAC@MM (10 mg kg^{-1}) at 6, 12, 24, 30, 48, 54, 72, 78 h).

pro-inflammation cytokine) as determined by IHC analysis. All these investigations validate that BH-EGCG&NAC@MM can target and accumulate in the inflamed paw, and effectively suppress inflammation, thus resulting in the attenuation of hind paw edema.

Afterwards, we proceeded to employ BH-EGCG&NAC@MM for treating autoimmune hepatitis in the ConA-induced AIH mouse model. Similarly, the mice were randomly divided into 6 groups (G1-G6) and administered with different therapeutic formulations according to the experimental outline shown in Fig. 6A. G1 was the heathy mice treated with saline, G2 was the ConA-induced AIH model mice treated with saline, G3 was the ConA-induced AIH model mice treated with free EGCG, G4 was the ConA-induced AIH model mice treated with free NAC, G5 was the ConA-induced AIH model mice treated with BH-EGCG and free NAC, G6 was the ConA-induced AIH model mice treated with BH-EGCG&NAC@MM. Fig. 6B and D and Figs. S38–39 display the NIR fluorescent images and MSOT images of the mice acquired at 30 min post injection (i.v.) of BH-EGCG&NAC@MM after receiving 4 or 8 therapeutic injections. The mean intensities of ROI covering the whole liver regions of the mice from G1-G6 are given in Fig. 6C and E. It is easily found that the fluorescent and optoacoustic intensities in the liver regions of the mice after receiving 8 therapeutic injections (at 92 h) are weaker than those mice after receiving 4 therapeutic injection (at 44 h), indicating that therapeutic efficacy is significantly improved as the times of therapeutic injections increases. Similarly, the fluorescent and optoacoustic signals in G6 is the weakest compared to those in other treatment groups (G2-G5), suggesting the best therapeutic effect of BH-EGCG&NAC@MM. G3-G5 also show a certain degree of decrease in fluorescent and optoacoustic intensities. Additionally, the serum levels of ALT and typical inflammatory cytokine (IL-1β) from G1-G6 were also measured after 8 therapeutic injections, as shown in Fig. 6F and Fig. S40. The data confirm the best therapeutic efficacy of BH-EGCG&NAC@MM among the treatment groups. Moreover, the liver sections from the mice in G1-G6 underwent histological (H&E staining) and IHC analyses. As displayed in Fig. 6G and Fig. S41, the morphology in G2 is the most abnormal, showing massive hepatocyte necrosis and obvious inflammatory infiltration. However, different degrees of suppression of hepatocyte necrosis and inflammatory infiltration can be observed in the liver sections from G3-G6, and G6 shows the best recovery in tissue morphology. From the IHC analysis, similarly, we can see that IL-6 expression in G6 is lower than those in G2-G5. These observations substantiate the imaging results and also demonstrate that BH-EGCG&NAC@MM exhibits the best therapeutic outcomes.

Inflammasome is an important component of the congenital immune system and plays crucial role in regulating immune-mediated inflammatory diseases [26–28]. Among NLR inflammasome complexes, the NLRP3 inflammasome has been the most widely characterized and is a crucial signaling node, which consists of NLRP3, apoptosis-associated speck-like protein (ASC) and procaspase-1. Activation of the NLRP3 inflammasome requires two sequential steps (priming and assembling) which are trigged by two signals, so as to upregulate the expression of the pattern recognition receptor NLRP3 and induce the assembly of NLRP3 inflammasome. NF-κB is a transcription factor that is essential for inflammatory responses and for upregulating NLRP3 protein synthesis. To elucidate whether the therapeutic effects of BH-EGCG&NAC@MM for autoimmune hepatitis is achieved through inhibition of NF-κB signaling pathway and NLPR3 inflammasome activities, we performed Western blotting analyses for the liver tissues from different groups of mice, and the results are shown in Fig. 6H. For G1, both NF-κB p65 and cytoplasmic NLRP3 inflammasome levels are quite low, suggesting in healthy liver these signaling pathways mostly remain inactive. For G2, it is clear that both cytoplasmic NLRP3 inflammasome and NF-κB P65 levels are quite high, indicating the autoimmune hepatitis is closely associated with NF-κB and NLRP3 inflammasome activation. While in G6, the NF-κB and NLRP3 inflammasome levels decrease obviously to the levels comparable to those in G1. The results signify that BH-EGCG&NAC@MM rehabilitates autoimmune hepatitis through

inhibiting NF-κB signaling pathway and suppressing NLRP3 inflammasome activation.

In this study, the nanosystem (BH-EGCG&NAC@MM) can actively target the inflammation site and release two drugs (NAC and EGCG) under the stimulation of overexpressed ROS (H_2O_2). On one hand, the released EGCG inhibits NF-κB signaling via decreasing the phosphorylation of IκB kinase [29–31], thus reducing the expression of transcription factor NF-κB. The inhibition of NF-κB leads to the reduced production of inflammatory cytokines as well as the pattern recognition receptor NLRP3 [32]. On the other hand, the released EGCG can reduce the level of ROS owing to its antioxidant feature, thus further suppressing the activation of NLRP3 inflammasome. On another front, the released drug NAC, known as an antioxidant precursor and scavenger of ROS, can also reduce ROS levels and inhibit the apoptosis associated with H_2O_2 [78], which contributes to reducing the inflammation and achieving the therapeutic efficacy, as shown in Fig. 1. The main limitation for this nanosystem lies in its relatively short absorption/emission wavelength. Extending the absorption/emission into the second near-infrared window would improve the imaging performance, and the potential applications of the nanosystem and its derivatives (e.g., nanoparticles loaded with other drugs or containing other-biomarker responsive units) may be further explored for other diseases in future.

4. Conclusion

In summary, we have developed a ROS-activatable and targeted nanosystem for detecting and imaging two immune-inflammatory diseases (CAR-induced hind paw edema and ConA-induced autoimmune hepatitis), as well as for treating these diseases via inhibiting NF-κB signaling pathway and suppressing the NLRP3 inflammasome activity. Benefiting from the macrophage membrane's inflammation-homing effect, the macrophage membrane-coated nanoparticles can effectively target inflammatory disease sites. Upon responding to the overexpressed ROS in inflammatory lesions, the nanosystem releases the NIR chromophore to generate fluorescence and MSOT signals for dual-mode imaging. Furthermore, the released drugs (NAC and EGCG) can exert therapeutic actions via inhibiting NF-κB signaling pathway and suppressing the NLRP3 inflammasome activity. The approach herein would provide insightful information for contriving other targeted theranostic nonosystems for various immune-mediated inflammatory diseases.

CRediT authorship contribution statement

Lihe Sun: Conceptualization, Methodology, Investigation, Formal analysis, Writing – original draft. **Juan Ouyang:** Conceptualization, Methodology, Investigation, Formal analysis, Writing – original draft. **Zhuo Zeng:** Investigation, Methodology, Validation. **Cheng Zeng:** Investigation, Methodology, Validation. **Yunqing Ma:** Investigation, Methodology, Validation. **Fang Zeng:** Conceptualization, Formal analysis, Project administration, Funding acquisition, Supervision, Resources, Writing – review & editing. **Shuizhu Wu:** Conceptualization, Formal analysis, Project administration, Funding acquisition, Supervision, Resources, Writing – review & editing.

Declaration of competing interest

The authors declare that they have no known competing financial interests or personal relationships that could have appeared to influence the work reported in this paper.

Acknowledgments

Appendix A. Supplementary data

Supplementary data to this article can be found online at https://doi.org/10.1016/j.bioactmat.2021.08.010.

References

[1] W.E. Ruff, T.M. Greiling, M.A. Kriegel, Host-microbiota interactions in immune-mediated diseases, Nat. Rev. Microbiol. 18 (2020) 521–538, https://doi.org/10.1038/s41579-020-0367-2.

[2] N.J. Bernard, Preventing immune-complex-mediated disease, Nat. Rev. Rheumatol. 15 (2019) 4, https://doi.org/10.1038/s41584-018-0137-y.

[3] C. Cotsapas, D.A. Hafler, Immune-mediated disease genetics: the shared basis of pathogenesis, Trends, Immunol. 34 (2013) 22–26, https://doi.org/10.1016/j.it.2012.09.001.

[4] A. Kuek, B.L. Hazleman, A.J. Ostor, Immune-mediated inflammatory diseases (IMIDs) and biologic therapy: a medical revolution, Postgrad. Med. 83 (2007) 251–260, https://doi.org/10.1136/pgmj.2006.052688.

[5] H.H. Chen, W.C. Chao, Y.H. Chen, T.Y. Hsieh, K.L. Lai, Y.M. Chen, W.T. Hung, C. T. Lin, C.W. Tseng, C.H. Lin, Risk of immune-mediated inflammatory diseases in newly diagnosed ankylosing spondylitis patients: a population-based matched cohort study, Arthritis Res. Ther. 21 (2019) 196, https://doi.org/10.1186/s13075-019-1980-1.

[6] D. Aletaha, A.J. Epstein, M. Skup, P. Zueger, V. Garg, R. Panaccione, Risk of developing additional immune-mediated manifestations: a retrospective matched cohort study, Adv. Ther. 36 (2019) 1672–1683, https://doi.org/10.1007/s12325-019-00964-z.

[7] K.F. Baker, J.D. Isaacs, Novel therapies for immune-mediated inflammatory diseases: what can we learn from their use in rheumatoid arthritis, spondyloarthritis, systemic lupus erythematosus, psoriasis, crohn's disease and ulcerative colitis? Ann. Rheum. Dis. 77 (2018) 175–187, https://doi.org/10.1136/annrheumdis-2017-211555.

[8] G.E. Fragoulis, I.B. McInnes, S. Siebert, JAK-inhibitors. new players in the field of immune-mediated diseases, beyond rheumatoid arthritis, Rheumatology 58 (2019) i43–i54, https://doi.org/10.1093/rheumatology/key276.

[9] H. Wang, X. Feng, P. Han, Y. Lei, Y. Xia, D. Tian, W. Yan, The JAK inhibitor tofacitinib ameliorates immune-mediated liver injury in mice, Mol. Med. Rep. 20 (2019) 4883–4892, https://doi.org/10.3892/mmr.2019.10750.

[10] F. Sahebjam, J.M. Vierling, Autoimmune hepatitis, Front. Med. 9 (2015) 187–219, https://doi.org/10.1007/s11684-015-0386-y.

[11] J. Korzenik, M.D. Larsen, J. Nielsen, J. Kjeldsen, B.M. Nørgård, Increased risk of developing crohn's disease or ulcerative colitis in 17018 patients while under treatment with anti-TNFα agents, particularly etanercept, for autoimmune diseases other than inflammatory bowel disease, Aliment. Pharmacol. Ther. 50 (2019) 289–294, https://doi.org/10.1111/apt.15370.

[12] M. Kubo, Innate and adaptive type 2 immunity in lung allergic inflammation, Immunol. Rev. 278 (2017) 162–172, https://doi.org/10.1111/imr.12557.

[13] J. Burisch, T. Jess, A. Egeberg, Incidence of immune-mediated inflammatory diseases among patients with inflammatory bowel diseases in Denmark, Clin. Gastroenterol. Hepatol. 17 (2019) 2704–2712, https://doi.org/10.1016/j.cgh.2019.03.040.

[14] L. Antonioli, C. Blandizzi, P. Pacher, G. Haskó, The purinergic system as a pharmacological target for the treatment of immune-mediated inflammatory diseases, Pharmacol. Rev. 71 (2019) 345–382, https://doi.org/10.1124/pr.117.014878.

[15] J.S. Smolen, R. Landewé, J. Bijlsma, G. Burmester, K. Chatzidionysiou, M. Dougados, J. Nam, S. Ramiro, M. Voshaar, R. van Vollenhoven, D. Aletaha, M. Aringer, M. Boers, C.D. Buckley, F. Buttgereit, V. Bykerk, M. Cardiel, B. Combe, M. Cutolo, Y. van Eijk-Hustings, P. Emery, A. Finckh, C. Gabay, J. Gomez-Reino, L. Gossec, J.E. Gottenberg, J.M.W. Hazes, T. Huizinga, M. Jani, D. Karateev, M. Kouloumas, T. Kvien, Z. Li, X. Mariette, I. McInnes, E. Mysler, P. Nash, K. Pavelka, G. Poór, C. Richez, P. van Riel, A. Rubbert-Roth, K. Saag, J. da Silva, T. Stamm, T. Takeuchi, R. Westhovens, M. de Wit, D. van der Heijde, EULAR recommendations for the management of rheumatoid arthritis with synthetic and biological disease-modifying antirheumatic drugs: 2016 update, Ann. Rheum. Dis. 76 (2017) 960–977, https://doi.org/10.1136/annrheumdis-2016-210715.

[16] J.A. Singh, A. Hossain, E. Tanjong Ghogomu, A.S. Mudano, P. Tugwell, G.A. Wells, Biologic or tofacitinib monotherapy for rheumatoid arthritis in people with traditional disease-modifying anti-rheumatic drug (DMARD) failure: a cochrane systematic review and network meta-analysis (NMA), Cochrane Database Syst. Rev. 11 (2016) CD012437, https://doi.org/10.1002/14651858.CD012437.

[17] D.E. Furst, E.C. Keystone, A.K. So, J. Braun, F.C. Breedveld, G.R. Burmester, F. De Benedetti, T. Dörner, P. Emery, R. Fleischmann, A. Gibofsky, J.R. Kalden, A. Kavanaugh, B. Kirkham, P. Mease, A. Rubbert-Roth, J. Sieper, N.G. Singer, J. S. Smolen, P.L. Van Riel, M.H. Weisman, K.L. Winthrop, Updated consensus statement on biological agents for the treatment of rheumatic diseases, Ann. Rheum. Dis. 72 (2012) ii2–ii34, https://doi.org/10.1136/annrheumdis-2013-203348, 2013.

[18] F. Cantini, L. Niccoli, D. Goletti, Tuberculosis risk in patients treated with non-anti-tumor necrosis factor-α (TNF-α) targeted biologics and recently licensed TNF-α inhibitors: data from clinical trials and national registries, J. Rheumatol. Suppl. 91 (2014) 56–64, https://doi.org/10.3899/jrheum.140103.

[19] J. Jegatheeswaran, M. Turk, J.E. Pope, Comparison of janus kinase inhibitors in the treatment of rheumatoid arthritis: a systemic literature review, Immunotherapy 11 (2019) 737–754, https://doi.org/10.2217/imt-2018-0178.

[20] H. Kim, S. Dill, M. O`Brien, L. Vian, X. Li, M. Manukyan, M. Jain, L.W. Adeojo, J. George, M. Perez, A.A. Grom, M. Sutter, B.M. Feldman, L. Yao, M. Millwood, A. Brundidge, D.C. Pichard, E.W. Cowen, Y. Shi, S. Lu, W.L. Tsai, M. Gadina, L. G. Rider, R.A. ColbertM, Janus kinase (JAK) inhibition with baricitinib in refractory juvenile dermatomyositis, Ann. Rheum. Dis. 80 (2021) 406–408, https://doi.org/10.1136/annrheumdis-2020-218690.

[21] D. Klatzmann, A.K. Abbas, The promise of low-dose interleukin-2 therapy for autoimmune and inflammatory diseases, Nat. Rev. Immunol. 15 (2015) 283–294, https://doi.org/10.1038/nri3823.

[22] B. Briard, T. Fontaine, P. Samir, D.E. Place, L. Muszkieta, R.K.S. Malireddi, R. Karki, S. Christgen, P. Bomme, P. Vogel, R. Beau, E. Mellado, O. Ibrahim-Granet, B. Henrissat, R.C. Kalathur, C. Robinson, J.P. Latgé, T.D. Kanneganti, Galactosaminogalactan activates the inflammasome to provide host protection, Nature 588 (2020) 688–692, https://doi.org/10.1038/s41586-020-2996-z.

[23] B. Briard, R. Karki, R.K.S. Malireddi, A. Bhattacharya, D.E. Place, J. Mavuluri, J. L. Peters, P. Vogel, M. Yamamoto, T.D. Kanneganti, Fungal ligands released by innate immune effectors promote inflammasome activation during aspergillus fumigatus infection, Nat. Microbiol. 4 (2019) 316–327, https://doi.org/10.1038/s41564-018-0298-0.

[24] K. Zheng, J. Bai, N. Li, M. Li, H. Sun, W. Zhang, G. Ge, X. Liang, H. Tao, Y. Xue, Y. Hao, C. Zhu, Y. Xu, D. Geng, Protective effects of sirtuin 3 on titanium particle-induced osteogenic inhibition by regulating the NLRP3 inflammasome via the GSK-3β/β-catenin signalling pathway, Bioact. Mater. 6 (2021) 3343–3357, https://doi.org/10.1016/j.bioactmat.2021.02.039.

[25] A. Abderrazak, T. Syrovets, D. Couchie, K. El Hadri, B. Friguet, T. Simmet, M. Rouis, NLRP3 inflammasome: from a danger signal sensor to a regulatory node of oxidative stress and inflammatory diseases, Redox. Biol. 4 (2015) 296–307, https://doi.org/10.1016/j.redox.2015.01.008.

[26] K.V. Swanson, M. Deng, J.P. Ting, The NLRP3 inflammasome: molecular activation and regulation to therapeutics, Nat. Rev. Immunol. 19 (2019) 477–489, https://doi.org/10.1038/s41577-019-0165-0.

[27] S. Lemprière, NLRP3 inflammasome activity as biomarker for primary progressive multiple sclerosis, Nat. Rev. Neurol. 16 (2020), https://doi.org/10.1038/s41582-020-0366-y, 350-350.

[28] C. Ising, C. Venegas, S. Zhang, H. Scheiblich, S.V. Schmidt, A. Vieira-Saecker, S. Schwartz, S. Albasset, R.M. McManus, D. Tejera, A. Griep, F. Santarelli, F. Brosseron, S. Opitz, J. Stunden, M. Merten, R. Kayed, D.T. Golenbock, D. Blum, E. Latz, L. Buée, M.T. Heneka, NLRP3 inflammasome activation drives tau pathology, Nature 575 (2019) 669–673, https://doi.org/10.1038/s41586-019-1769-z.

[29] M.S.J. Mangan, E.J. Olhava, W.R. Roush, H.M. Seidel, G.D. Glick, E. Latz, Targeting the NLRP3 inflammasome in inflammatory diseases, Nat. Rev. Drug Discov. 17 (2018) 588–606, https://doi.org/10.1038/nrd.2018.97.

[30] F. Wan, M.J. Lenardo, The nuclear signaling of NF-κB: current knowledge, new insights, and future perspectives, Cell Res. 20 (2010) 24–33, https://doi.org/10.1038/cr.2009.137.

[31] K.C. Choi, M.G. Jung, Y.H. Lee, J.C. Yoon, S.H. Kwon, H.B. Kang, M.J. Kim, J. H. Cha, Y.J. Kim, W.J. Jun, J.M. Lee, H.G. Yoon, Epigallocatechin-3-gallate, a histone acetyltransferase inhibitor, inhibits EBV-induced B lymphocyte transformation via suppression of RelA acetylation, Canc. Res. 69 (2009) 583–592, https://doi.org/10.1158/0008-5472.CAN-08-2442.

[32] M.D. McGeough, A. Wree, M.E. Inzaugarat, A. Haimovich, C.D. Johnson, C.A. Peña, R. Goldbach-Mansky, L. Broderick, A.E. Feldstein, H.M. Hoffman, TNF regulates transcription of NLRP3 inflammasome components and inflammatory molecules in cryopyrinopathies, J. Clin. Invest. 127 (2017) 4488–4497, https://doi.org/10.1172/JCI90699.

[33] J.J. Zhang, C.C. Lu, G.C. Yen, Epigallocatechin gallate inhibits urate crystals-induced peritoneal inflammation in C57BL/6 mice, Mol. Nutr. Food Res. 60 (2016) 2297–2303, https://doi.org/10.1002/mnfr.201600106.

[34] D. Wang, Q. Gao, T. Wang, Z. Kan, X. Li, L. Hu, C.Y. Peng, F. Qian, Y. Wang, D. Granato, Green tea polyphenols and epigallocatechin-3-gallate protect against perfluorodecanoic acid induced liver damage and inflammation in mice by inhibiting NLRP3 inflammasome activation, Food Res. Int. 127 (2020) 108628, https://doi.org/10.1016/j.foodres.2019.108628.

[35] R. Kanlaya, V. Thongboonkerd, Molecular mechanisms of epigallocatechin-3-gallate for prevention of chronic kidney disease and renal fibrosis: preclinical evidence, Curr. Dev. Nutr. 3 (2019), https://doi.org/10.1093/cdn/nzz101 nzz101.

[36] V. Pucino, D. Cucchi, C. Mauro, Lactate transporters as therapeutic targets in cancer and inflammatory diseases, Expert Opin. Ther. Targets 22 (2018) 735–743, https://doi.org/10.1080/14728222.2018.1511706.

[37] S. Zhang, J. Ermann, M.D. Succi, A. Zhou, M.J. Hamilton, B. Cao, J.R. Korzenik, J. N. Glickman, P.K. Vemula, L.H. Glimcher, G. Traverso, R. Langer, J.M. Karp, An inflammation-targeting hydrogel for local drug delivery in inflammatory bowel disease, Sci. Transl. Med. 7 (2015), https://doi.org/10.1126/scitranslmed.aaa5657, 300ra128-300ra128.

[38] L. Shen, S. Tenzer, W. Storck, D. Hobernik, V.K. Raker, K. Fischer, S. Decker, A. Dzionek, S. Krauthäuser, M. Diken, A. Nikolaev, J. Maxeiner, P. Schuster, C. Kappel, A. Verschoor, H. Schild, S. Grabbe, M. Bros, Protein corona-mediated targeting of nanocarriers to B cells allows redirection of allergic immune responses, J. Allergy Clin. Immunol. 142 (2018) 1558–1570, https://doi.org/10.1016/j.jaci.2017.08.049.

[39] D. Dehaini, X. Wei, R.H. Fang, S. Masson, P. Angsantikul, B.T. Luk, Y. Zhang, M. Ying, Y. Jiang, A.V. Kroll, W. Gao, L. Zhang, Erythrocyte-platelet hybrid

membrane coating for enhanced nanoparticle functionalization, Adv. Mater. 29 (2017) 1606209, https://doi.org/10.1002/adma.201606209.

[40] H.H. Wu, Y. Zhou, Y. Tabata, J.Q. Gao, Mesenchymal stem cell-based drug delivery strategy: from cells to biomimetic, J. Contr. Release 294 (2019) 102–113, https://doi.org/10.1016/j.jconrel.2018.12.019.

[41] A. Narain, S. Asawa, V. Chhabria, Y. Patil-Sen, Cell membrane coated nanoparticles: next-generation therapeutics, Nanomedicine 12 (2017) 2677–2692, https://doi.org/10.2217/nnm-2017-0225.

[42] G. Deng, Z. Sun, S. Li, X. Peng, W. Li, L. Zhou, Y. Ma, P. Gong, L. Cai, Cell-membrane immunotherapy based on natural killer cell membrane coated nanoparticles for the effective inhibition of primary and abscopal tumor growth, ACS Nano 12 (2018) 12096–12108, https://doi.org/10.1021/acsnano.8b05292.

[43] C. Matyas, G. Hasko, L. Liaudet, E. Trojnar, P. Pacher, Interplay of cardiovascular mediators, oxidative stress and inflammation in liver disease and its complications, Nat. Rev. Cardiol. 18 (2021) 117–135, https://doi.org/10.1038/s41569-020-0433-5.

[44] A.R. Bourgonje, M. Feelisch, K.N. Faber, A. Pasch, G. Dijkstra, H. van Goor, Oxidative stress and redox-modulating therapeutics in inflammatory bowel disease, Trends Mol. Med. 26 (2020) 1034–1046, https://doi.org/10.1016/j.molmed.2020.06.006.

[45] S. Zhang, Y. Li, X. Qiu, A. Jiao, W. Luo, X. Lin, X. Zhang, Z. Zhang, J. Hong, P. Cai, Y. Zhang, Y. Wu, J. Gao, C. Liu, Y. Li, Incorporating redox-sensitive nanogels into bioabsorbable nanofibrous membrane to acquire ROS-balance capacity for skin regeneration, Bioact. Mater. 6 (2021) 3461–3472, https://doi.org/10.1016/j.bioactmat.2021.03.009.

[46] K. Sachdeva, D.C. Do, Y. Zhang, X. Hu, J. Chen, P. Gao, Environmental exposures and asthma development: autophagy, mitophagy, and cellular senescence, Front. Immunol. 10 (2019) 2787, https://doi.org/10.3389/fimmu.2019.02787.

[47] M.J. Smallwood, A. Nissim, A.R. Knight, M. Whiteman, R. Haigh, P.G. Winyard, Oxidative stress in autoimmune rheumatic diseases, Free Radic. Biol. Med. 125 (2018) 3–14, https://doi.org/10.1016/j.freeradbiomed.2018.05.086.

[48] Z. Chen, J. Duan, Y. Diao, Y. Chen, X. Liang, H. Li, Y. Miao, Q. Gao, L. Gui, X. Wang, J. Yang, Y. Li, ROS-responsive capsules engineered from EGCG-Zinc networks improve therapeutic angiogenesis in mouse limb ischemia, Bioact. Mater. 6 (2021) 1–11, https://doi.org/10.1016/j.bioactmat.2020.07.013.

[49] G. Chen, H. Deng, X. Song, M. Lu, L. Zhao, S. Xia, G. You, J. Zhao, Y. Zhang, A. Dong, H. Zhou, Reactive oxygen species-responsive polymeric nanoparticles for alleviating sepsis-induced acute liver injury in mice, Biomaterials 144 (2017) 30–41, https://doi.org/10.1016/j.biomaterials.2017.08.008.

[50] W.X. Wang, W.L. Jiang, G.J. Mao, M. Tan, J. Fei, Y. Li, C.Y. Li, Monitoring the fluctuation of hydrogen peroxide in diabetes and its complications with a novel near-infrared fluorescent probe, Anal. Chem. 93 (2021) 3301–3307, https://doi.org/10.1021/acs.analchem.0c05364.

[51] J. Ouyang, L.H. Sun, Z. Zeng, C. Zeng, F. Zeng, S.Z. Wu, Nanoaggregate probe for breast cancer metastasis through multispectral optoacoustic tomography and aggregation-induced NIR-I/II fluorescence imaging, Angew. Chem. Int. Ed. 59 (2020) 10111–10121, https://doi.org/10.1002/anie.201913149.

[52] L. Zhang, W. Che, Z. Yang, X. Liu, S. Liu, Z. Xie, D. Zhu, Z. Su, B. Tang, M.R. Bryce, Bright red aggregation-induced emission nanoparticles for multifunctional applications in cancer therapy, Chem. Sci. 11 (2020) 2369–2374, https://doi.org/10.1039/C9SC06310B.

[53] M. Xu, R. Li, X. Li, G. Lv, S. Li, A. Sun, Y. Zhou, T. Yi, NIR fluorescent probes with good water-solubility for detection of amyloid beta aggregates in alzheimer's disease, J. Mater. Chem. B. 7 (2019) 5535–5540, https://doi.org/10.1039/c9tb01012b.

[54] W.L. Jiang, W.X. Wang, G.J. Mao, L. Yan, Y. Du, Y. Li, C.Y. Li, Construction of NIR and ratiometric fluorescent probe for monitoring carbon monoxide under oxidative stress in zebrafish, Anal. Chem. 93 (2021) 2510–2518, https://doi.org/10.1021/acs.analchem.0c04537.

[55] J. Wang, L. Sui, J. Huang, L. Miao, Y. Nie, K. Wang, Z. Yang, Q. Huang, X. Gong, Y. Nan, K. Ai, MoS₂-based nanocomposites for cancer diagnosis and therapy, Bioact. Mater. 6 (2021) 4209–4242, https://doi.org/10.1016/j.bioactmat.2021.04.021.

[56] Y. Li, Y. Zhou, X. Yue, Z. Dai, Cyanine conjugates in cancer theranostics, Bioact. Mater. 6 (2021) 794–809, https://doi.org/10.1016/j.bioactmat.2020.09.009.

[57] N. Beziere, N. Lozano, A. Nunes, J. Salichs, D. Queiros, K. Kostarelos, V. Ntziachristos, Dynamic imaging of PEGylated indocyanine green (ICG) liposomes within the tumor microenvironment using multi-spectral optoacoustic tomography (MSOT), Biomaterials 37 (2015) 415–424, https://doi.org/10.1016/j.biomaterials.2014.10.014.

[58] Z. Fan, H. Liu, Y. Xue, J. Lin, Y. Fu, Z. Xia, D. Pan, J. Zhang, K. Qiao, Z. Zhang, Y. Liao, Reversing cold tumors to hot: an immunoadjuvant-functionalized metal-organic framework for multimodal imaging-guided synergistic photo-immunotherapy, Bioact. Mater. 6 (2021) 312–325, https://doi.org/10.1016/j.bioactmat.2020.08.005.

[59] Y. Tian, W.L. Jiang, W.X. Wang, G.J. Mao, Y. Li, C.Y. Li, NAD(P)H-triggered probe for dual-modal imaging during energy metabolism and novel strategy of enhanced photothermal therapy in tumor, Biomaterials 271 (2021) 120736, https://doi.org/10.1016/j.biomaterials.2021.120736.

[60] Y. Wu, S. Huang, J. Wang, L. Sun, F. Zeng, S. Wu, Activatable probes for diagnosing and positioning liver injury and metastatic tumors by multispectral optoacoustic tomography, Nat. Commun. 9 (2018) 3983, https://doi.org/10.1038/s41467-018-06499-1.

[61] Y. Wu, F. Zeng, Y. Zhao, S. Wu, Emerging contrast agents for multispectral optoacoustic imaging and their biomedical applications, Chem. Soc. Rev. 50 (2021) 7924–7940, https://doi.org/10.1039/d1cs00358e.

[62] H. Zhuang, B. Li, M. Zhao, P. Wei, W. Yuan, M. Zhang, X. Han, Y. Chen, T. Yi, Real-time monitoring and accurate diagnosis of drug-induced hepatotoxicity in vivo by ratio-fluorescence and photoacoustic imaging of peroxynitrite, Nanoscale 12 (2020) 10216–10225, https://doi.org/10.1039/d0nr00963f.

[63] J. Chen, Y. Fang, L. Sun, F. Zeng, S. Wu, An activatable probe for detecting alcoholic liver injury via multispectral optoacoustic tomography and fluorescence imaging, Chem. Commun. 56 (2020) 11102–11105, https://doi.org/10.1039/D0CC04635C.

[64] H.W. Liu, X.X. Hu, K. Li, Y. Liu, Q. Rong, L. Zhu, L. Yuan, F.L. Qu, X.B. Zhang, W. Tan, A mitochondrial-targeted prodrug for NIR imaging guided and synergetic NIR photodynamic-chemo cancer therapy, Chem. Sci. 8 (2017) 7689–7695, https://doi.org/10.1039/c7sc03454g.

[65] M. Wang, X. Cai, J. Yang, C. Wang, L. Tong, J. Xiao, L. Li, A targeted and pH-responsive bortezomib nanomedicine in the treatment of metastatic bone tumors, ACS Appl. Mater. Interfaces 10 (2018) 41003–41011, https://doi.org/10.1021/acsami.8b07527.

[66] S. Thamphiwatana, P. Angsantikul, T. Escajadillo, Q. Zhang, J. Olson, B.T. Luk, S. Zhang, R.H. Fang, W. Gao, V. Nizet, L. Zhang, Macrophage-like nanoparticles concurrently absorbing endotoxins and proinflammatory cytokines for sepsis management, Proc. Natl. Acad. Sci. Unit. States Am. 114 (2017) 11488–11493, https://doi.org/10.1073/pnas.1714267114.

[67] C. Gao, Q. Huang, C. Liu, C.H.T. Kwong, L. Yue, J.B. Wan, S.M.Y. Lee, R. Wang, Treatment of atherosclerosis by macrophage-biomimetic nanoparticles via targeted pharmacotherapy and sequestration of proinflammatory cytokines, Nat. Commun. 11 (2020) 2622, https://doi.org/10.1038/s41467-020-16439-7.

[68] C. Wang, Y. Wang, L. Zhang, R.J. Miron, J. Liang, M. Shi, W. Mo, S. Zheng, Y. Zhao, Y. Zhang, Pretreated macrophage-membrane-coated gold nanocages for precise drug delivery for treatment of bacterial infections, Adv. Mater. 30 (2018) 1804023, https://doi.org/10.1002/adma.201804023.

[69] L. Wang, W. Zhang, C.H. Ge, R.H. Yin, Y. Xiao, Y.Q. Zhan, M. Yu, C.Y. Li, Z.Q. Ge, X.M. Yang, Toll-like receptor 5 signaling restrains T-cell/natural killer T-cell activation and protects against concanavalin A-induced hepatic injury, Hepatology 65 (2017) 2059–2073, https://doi.org/10.1002/hep.29140.

[70] K. Nakamura, T. Ito, M. Yoneda, S. Takamoto, Y. Nakade, S. Okamoto, M. Okada, S. Yokohama, K. Aso, I. Makino, Antithrombin III prevents concanavalin A-induced liver injury through inhibition of macrophage inflammatory protein-2 release and production of prostacyclin in mice, J. Hepatol. 36 (2002) 766–773, https://doi.org/10.1016/s0168-8278(02)00059-4.

[71] P. Zhang, Y. Yin, T. Wang, W. Li, C. Li, X. Zeng, W. Yang, R. Zhang, Y. Tang, L. Shi, R. Li, K. Tao, Maresin 1 mitigates concanavalin A-induced acute liver injury in mice by inhibiting ROS-mediated activation of NF-κB signaling, Free Radic. Biol. Med. 147 (2020) 23–36, https://doi.org/10.1016/j.freeradbiomed.2019.11.033.

[72] Q. Feng, J. Yao, G. Zhou, W. Xia, J. Lyu, X. Li, T. Zhao, G. Zhang, N. Zhao, J. Yang, Quantitative proteomic analysis reveals that arctigenin alleviates concanavalin A-induced hepatitis through suppressing immune system and regulating autophagy, Front. Immunol. 9 (2018) 1881, https://doi.org/10.3389/fimmu.2018.01881.

[73] A.K. Sharma, H. Singh, H. Chakrapani, Photocontrolled endogenous reactive oxygen species (ROS) generation, Chem. Commun. 55 (2019) 5259–5262, https://doi.org/10.1039/c9cc01747j.

[74] S. Cuzzocrea, B. Zingarelli, E. Gilad, P. Hake, A.L. Salzman, C. Szabó, Protective effect of melatonin in carrageenan-induced models of local inflammation: relationship to its inhibitory effect on nitric oxide production and its peroxynitrite scavenging activity, J. Pineal Res. 23 (1997) 106–116, https://doi.org/10.1111/j.1600-079x.1997.tb00342.x.

[75] R.F. Queiroz, A.K. Jordão, A.C. Cunha, V.F. Ferreira, M.R. Brigagão, A. Malvezzi, A.T. Amaral, O. Augusto, Nitroxides attenuate carrageenan-induced inflammation in rat paws by reducing neutrophil infiltration and the resulting myeloperoxidase-mediated damage, Free Radic. Biol. Med. 53 (2012) 1942–1953, https://doi.org/10.1016/j.freeradbiomed.2012.09.001.

[76] H. Beloeil, Z. Ababneh, R. Chung, D. Zurakowski, R.V. Mulkern, C.B. Berde, Effects of bupivacaine and tetrodotoxin on carrageenan-induced hind paw inflammation in rats (part 1): hyperalgesia, edema, and systemic cytokines, Anesthesiology 105 (2006) 128–138, https://doi.org/10.1097/00000542-200607000-00022.

[77] L. Mursaleen, B. Noble, S.H.Y. Chan, S. Somavarapu, M.G. Zariwala, N-acetylcysteine nanocarriers protect against oxidative stress in a cellular model of Parkinson's disease, Antioxidants 9 (2020) 600, https://doi.org/10.3390/antiox9070600.

[78] M. Halasi, M. Wang, T.S. Chavan, V. Gaponenko, N. Hay, A.L. Gartel, ROS inhibitor N-acetyl-L-cysteine antagonizes the activity of proteasome inhibitors, Biochem. J. 454 (2013) 201–208, https://doi.org/10.1042/bj20130282.